Surprising behaviors in flapping locomotion with passive pitching

Saverio E. Spagnolie,[1,2] Lionel Moret,[1] Michael J. Shelley,[1] and Jun Zhang[1,3]
[1]*Applied Mathematics Laboratory, Courant Institute of Mathematical Sciences, New York University, New York, New York 10012, USA*
[2]*Department of Mechanical and Aerospace Engineering, University of California at San Diego, 9500 Gilman Drive, La Jolla, California 92093, USA*
[3]*Department of Physics, New York University, New York 10003, USA*

(Received 4 September 2009; accepted 25 February 2010; published online 30 April 2010)

To better understand the role of wing and fin flexibility in flapping locomotion, we study through experiment and numerical simulation a freely moving wing that can "pitch" passively as it is actively heaved in a fluid. We observe a range of flapping frequencies corresponding to large horizontal velocities, a regime of underperformance relative to a clamped (nonpitching) flapping wing, and a surprising, hysteretic regime in which the flapping wing can move horizontally in either direction (despite left/right symmetry being broken by the specific mode of pitching). The horizontal velocity is shown to peak when the flapping frequency is near the immersed system's resonant frequency. Unlike for the clamped wing, we find that locomotion is achieved by vertically flapped symmetric wings with even the slightest pitching flexibility, and the system exhibits a continuous departure from the Stokesian regime. The phase difference between the vertical heaving motion and consequent pitching changes continuously with the flapping frequency, and the direction reversal is found to correspond to a critical phase relationship. Finally, we show a transition from coherent to chaotic motion by increasing the wing's aspect ratio, and then a return to coherence for flapping bodies with circular cross section. © *2010 American Institute of Physics*. [doi:10.1063/1.3383215]

I. INTRODUCTION

The flapping of wings or fins is a common means of propulsion utilized by organisms as large as the blue whale (volume ≈ 100 m^3) and as small as the fairyfly (volume $\approx 10^{-9}$ m^3). Natural selection has driven the development of remarkable and efficient means of flapping locomotion, particularly in aquatic environments where the evolution of swimming propulsion has been (generally) unhindered by the requirements of weight support. The most efficient locomotion observed in such an environment is the thunniform mode of swimming as employed by teleost fish, sharks, and marine mammals.[1] In the thunniform mode, significant lateral body motions are generated only near the caudal fin, and the combination of both the lateral *heaving* and angular *pitching* leads to particularly efficient locomotive capabilities.[2,3]

The application of mathematical models to study swimming and flying is not a new endeavor, but many questions have yet to be fully answered. Of particular interest for the last few decades has been the interaction of flapping wings/fins with a viscous fluid, thrust/lift production via vorticity generation, and the effects of flexibility. Various experiments have been conducted with flapping foils in order to understand the underlying mechanisms in such systems. Extensive reviews of the literature and bibliographies may be found in Refs. 4–6. Most experiments that have been conducted focused on the active flapping of rigid foils, where the position and orientation are controlled, and the foil experiences an oncoming flow of constant velocity.

Unlike most man-made wings, real wings and fins in nature possess flexibility. It is widely agreed that the flexibility aids significantly in thrust generation, but our scientific understanding of precisely how is far from comprehensive. An early experimental study of flapping locomotion of insects and birds was conducted by Marey in 1869.[7] Marey used a freely moving, flexible apparatus to show, among many other fundamental aspects of locomotion in nature, that flight is only achieved in an intermediate regime of flapping frequencies. Moreover, he made note that in some circumstances the "experimental apparatus retrogrades and turns around its pivot in a direction contrary to its usual motion."[7] More recent steps toward understanding the effects of flexibility in flapping flight involved studying wings with a combination of vertical heaving and angular pitching.[8,9] It has been shown that under the right conditions, this forcing can lead to optimal propulsive performances, particularly when the motion is driven by a harmonic or sawtooth wave function.[10,11]

Vandenberghe, Zhang, and Childress[12] reintroduced an important element to the experimental study of flapping locomotion. Instead of studying bodies placed in an oncoming flow as in the recent works cited above, they studied a flapping wing that was free to move laterally relative to the flow, in the same spirit as Marey.[7] They showed that the simple sinusoidal heaving of a clamped (nonpitching) flapping wing is capable of breaking fluid symmetric response and can lead to coherent horizontal motion. By including this lateral degree of freedom, the authors were closer to matching biological systems, as birds and fish must produce their own forward (and generally unsteady) velocities through the flapping of wings or fins. This phenomenon was further analyzed numerically by Alben and Shelley.[13]

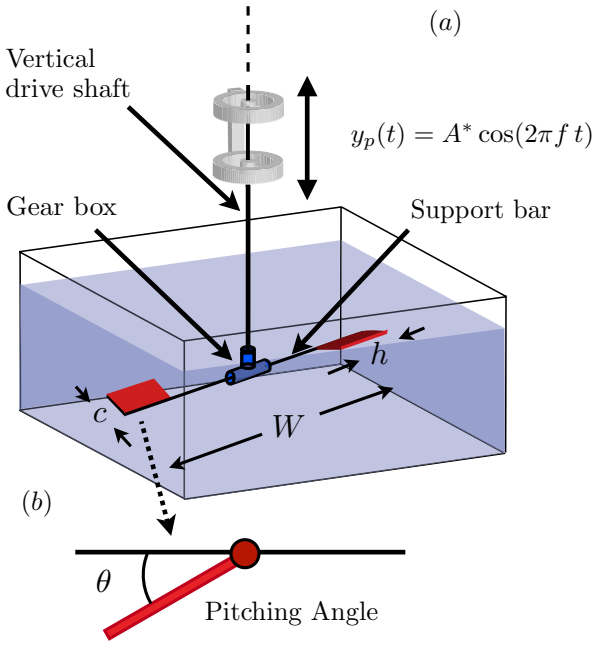

FIG. 1. (Color online) (a) The experimental setup. Two acrylic foils are connected by a support bar to a vertical drive shaft, which is driven vertically with a sinusoidal displacement. The foils both rotate around the central axis and twist equally about the support bar (passively) due to the fluid interactions, and due to a torsional spring inside the gear box which acts to return the foils to the horizontal plane. (b) The pitching angle θ.

To better understand the role of flexibility in flapping locomotion, we used the same experimental setup as in Ref. 12 to analyze the motion of a foil with a varying pitching angle, which varies passively based on interactions with the fluid. A torsional spring acts to restore the body toward the horizontal plane. The competition between this restorative torque and the fluid forces generated by the flapping motion provides a sufficient framework for generating many complex dynamical behaviors.

We first present the experimental setup and results which reveal the existence of two states of free flapping flight, "forward" and "backward," and show that the passive pitching introduces a hysteresis in the system. The phase difference between heaving and pitching is found to depend on the flapping frequency; furthermore, forward free flight corresponds to a phase difference smaller than π and backward free flight to a phase difference larger than π.

We then proceed to study numerically the Navier–Stokes equations in two dimensions, which are coupled to the equations for lateral and rotational accelerations of an elliptical wing. The wing is free to pitch passively about its rightmost edge with a torsional spring response to rotational deflections. The experimental results are reproduced qualitatively; we find a range of flapping frequencies corresponding to large horizontal (swimming) velocities, a regime of underperformance compared to a clamped flapping wing, and a regime where the pitching wing can move horizontally in either direction. The horizontal velocity is shown to peak when the flapping frequency is near the immersed system's resonant frequency. We confirm the experimentally observed critical phase difference between the heaving and consequent pitching that corresponds to this direction reversal. The numerical simulations allowed us to make predictions of other modes of flapping locomotion which were subsequently found in the experiments. In contrast with the dynamics of a flapping clamped wing,[12,13] we also find that locomotion occurs for bodies with even the slightest flexibility, providing a continuous departure from the Stokesian regime. Finally, we show a transition from coherent locomotion to chaotic motion by increasing the wing's aspect ratio, and then a return to coherence for bodies of circular cross section. A more comprehensive presentation of the experimental methods and observations will be provided in a separate work.

II. EXPERIMENTAL SETUP AND RESULTS

The experimental setup is presented in Fig. 1. In the study of freely moving wings, significant laboratory difficulties are introduced due to the large distances that such bodies may traverse; the rotational geometry in Fig. 1 approximates horizontal wing motion and allows for the consideration of arbitrarily large distances and times. Two acrylic rigid foils or "wings" extend from a vertical shaft at the center of a water-filled tank. The foils are connected to a support bar which is itself free to rotate around a vertical drive shaft. A gear and spring box connected to the base of the drive shaft is constructed so that the two wings are free to twist about the support bar as shown, and also to pitch in register (equally and simultaneously) at all times. A torsional spring internal to the gear box with spring constant κ^* acts to restore the wings to the horizontal plane, though the dynamic pitching angle is determined passively by the interaction of the body and its torsional spring with the surrounding fluid. The vertical drive shaft and support bar are driven to oscillate vertically by a direct-current motor with a sinusoidal displacement,

$$y_p(t) = A^* \cos(2\pi f t), \tag{1}$$

where A^* is the heaving amplitude and f is the frequency.

The acrylic wings have chord lengths $c=8$ cm, thickness $\delta=3$ mm, and span $h=13$ cm. The total span W of the two wing system is 46 cm. The square-based water tank is 20 cm deep and 57 cm wide, and is filled with water at room temperature. The shape of the tank has been found to have a negligible influence on the rotation speed. To suppress surface waves, the fluid surface is covered with a rigid lid with an opening in the center to accommodate the drive shaft (not shown). Surface waves are thus avoided and the top and bottom boundaries are flat. The fluid depth between the top and the bottom boundaries is made large enough to avoid "ground effects."

Figure 2 shows the angular velocity of the wings about the central axis, Ω, as a function of flapping frequency f for a heaving amplitude of $A^*=1.35$ cm and torsional spring constant $\kappa^*=0.15$ Nm/rad. Data for both the pitching and clamped wings (as studied in Ref. 12) are presented. The flapping clamped wing system is just as likely to rotate around the central axis in one direction as the other due to symmetry, and both branches of the mean rotational velocities are shown (see Refs. 12 and 13). As a flapped wing

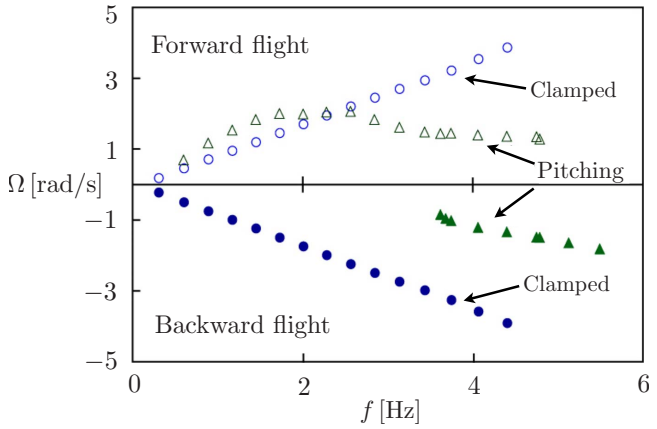

FIG. 2. (Color online) Experimental data comparing the vertical driving (flapping) frequency to the rotational velocity about the central axis (see Fig. 1) for a heaving amplitude of $A^*=1.35$ cm and torsional spring constant $\kappa^*=0.15$ Nm/rad. Data for both the pitching wing (triangles) and clamped wing (circles, as studied in Ref. 12) are presented.

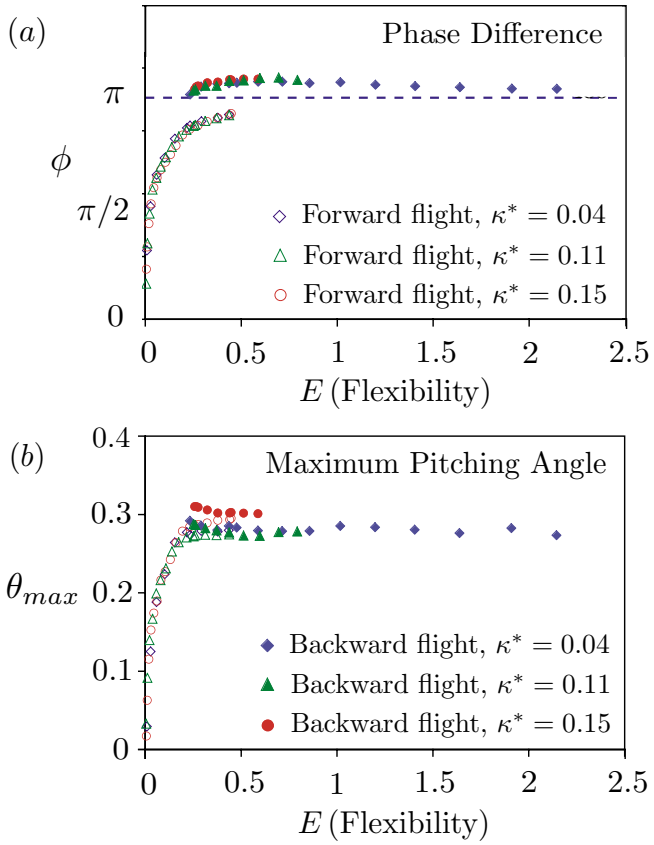

FIG. 3. (Color online) (a) Dependence of the phase difference ϕ on the dimensionless flexibility E (defined in the text). As the restorative torque exerted by the torsional spring decreases relative to the hydrodynamical torque, the phase difference increases in both forward and backward free flight. Remarkably, backward free flight (circles) is characterized by phase differences $\phi>\pi$ and forward free flight (filled circles) by $\phi<\pi$ (b) The average maximum pitching angle over one flapping period increases with flexibility in forward free flight and remains essentially constant in backward free flight.

moves forward, it produces a signature wake structure, a so-called inverted von Kármán street that is known to be associated with thrust generating bodies such as swimming fish[4] and birds.[12] In the case of the clamped wing, it has been observed that the horizontal spacing between the eddies associated with this flow structure does not change dramatically with the flapping frequency, which is analogous to the length between "footsteps."[12,14] Accordingly, the forward speed of a flapping clamped wing is in general linearly proportional to the flapping frequency.

In contrast, the pitching wing experiments show a range of flapping frequencies corresponding to increased locomotion velocities, a regime of underperformance relative to the clamped wing, and a bistable regime in which the flapping wing system can rotate in either direction. For small flapping frequencies, the pitching wings only move "forward," (in the direction of the wing edges connected to the support bar, or counterclockwise from above in Fig. 1), but there is a critical frequency beyond which the wings and support bar actually reverse their direction of rotation. Moreover, we observe a bistable regime in flapping frequency where the wings can move either forward or "backward" (clockwise from above in Fig. 1). The system also exhibits hysteresis; wings moving backward can be made to maintain this surprising direction of motion by slowly reducing the flapping frequency below the critical frequency for direction reversal.

To compare the relative effects of the fluid forces and the restorative torque, we define the dimensionless *flexibility* E as a ratio between the hydrodynamic torque on a wing plunging with velocity $2\pi A^* f$ to the torsional spring constant κ^*,

$$E=\frac{(1/2)C_d\rho h(2\pi A^* fc)^2}{\kappa^*}, \tag{2}$$

where ρ is the fluid density and C_d is the drag coefficient. Figure 3(a) shows the phase difference ϕ between the heaving and pitching for both forward free flight (filled shapes) and backward free flight (empty shapes) as a function of the flexibility E using torsional springs of three different stiffnesses. For purely sinusoidal motions the phase difference is defined implicitly by $\theta(t)=-\|\theta(t)\|_\infty\cos(2\pi ft-\phi)$; more generally we use the time lag between the zeroes $y_p(t_1)=0$ and $\theta(t_2)=0$ [with $\dot{y}_p(t_1)>0$ and $\dot{\theta}(t_2)>0$], setting $\phi=\pi-2\pi f(t_1-t_2)$. The phase difference is known to be a critical parameter for determining the flight efficiency when the pitching is controlled (see Refs. 9 and 10). In free flight with passive pitching the phase difference plays an even more interesting role. Our experiments show that ϕ increases continuously with flexibility in both forward and backward free flight. Furthermore, the transitions between forward and backward free flight correspond to transitions in ϕ below or above π, respectively. The phase difference maintains this dichotomy even through the bistable, hysteretic regime.

The relationship between ϕ and the direction of wing motion might be guessed by considering the wing kinematics shown in Fig. 4. Assuming purely sinusoidal motions, a phase difference of $\phi=\pi/2$ corresponds to kinematics in which a wing experiences its largest pitching (angular) velocity when the heaving displacement y_p is extremal. The heaving motion "leads" the pitching, and the free edge undergoes amplified vertical oscillations. In contrast, for phase differences $\phi>\pi$ the pitching leads the heaving, and the

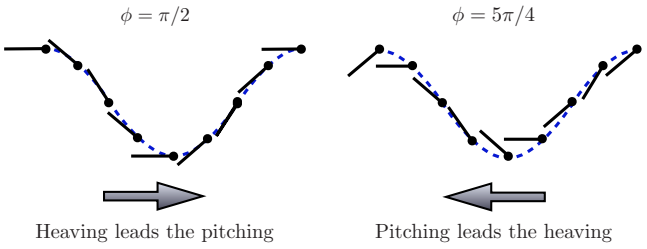

FIG. 4. (Color online) Kinematics associated with two phase differences between heaving and pitching oscillations. Phase differences $\phi<\pi$ correspond to forward free flight and $\phi>\pi$ to backward free flight (the flight direction is indicated by arrows). Circles indicate the position of the driving pivot.

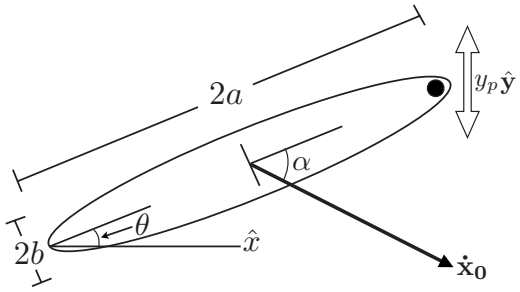

FIG. 5. The two-dimensional wing cross section is illustrated. The body is driven at the pivot point on the right with a vertical displacement $y_p(t)$. $\theta(t)$ is the angle between the elliptic major axis and the horizontal plane, and $\alpha(t)$ is the (attack) angle between the major axis and the direction of motion.

driven pivot edge experiences a larger vertical displacement than the free edge. The critical phase difference $\phi=\pi$ sees $y_p(t)$ and $\theta(t)$ reaching their extrema and zeroes simultaneously; the wing kinematics in this case exhibit fore/aft symmetry.

The dependence of the maximum pitching angle $\theta_{\max}$ on E is shown in Fig. 3(b). As expected, the maximum pitching angle increases with the flexibility in forward free flight. However, through the direction reversal transition and for backward free flight, the maximum pitching angle remains essentially constant. In addition to being characterized by a critical phase difference $\phi=\pi$, the direction reversal is also characterized by a maximum pitching angle of approximately 35° for the wing shape and flapping amplitude considered. Increased flexibility is achieved by either reducing the torsional spring strength or by increasing the flapping frequency. The dynamics of the flapping wing are the same in either case, as indicated in Fig. 3 where the data for three different spring constants fall onto nearly identical curves.

Many swimming organisms flap an appendage or expel fluid jets on a time scale which is at or near the relaxation time scale of their flexible fins or bodies. This has been shown recently for the swimming of such organisms as scallops,[15] tadpoles,[16] largemouth bass,[17] and squid.[18] It is natural to inquire about the hydrodynamic consequences of undulating or flapping near the resonant body frequency.

To address the possible relationship between input heaving frequency and resonant elastic frequency in the present system, we define a natural relaxation time of the wing in the absence of flapping. A relaxation time t_R is defined as the time required for an immersed wing with initial pitching angle $\theta=45°$, once released, to make its first return to the horizontal plane, $\theta=0$. The measured relaxation times using torsional springs with constants κ^* of 0.04, 0.11, and 0.15 Nm (those used in Fig. 3) are measured to be 1.02, 0.39, and 0.30 s, respectively. An approximate relationship in this regime of spring constants (in water) is thus $t_R \approx \gamma/\kappa^*$, with $\gamma=0.04$ Nm s. The associated resonant frequency is therefore $f_R=1/(4t_R)\approx\kappa^*/(4\gamma)$, which shows an apparent linear scaling in the torsional spring constant due to the fluid interaction, in contrast with the expected square-root relationship expected of an oscillating Hookean system in a vacuum. The resonant frequency so defined for the pitching wing used to create Fig. 2 is $f_R=0.83$ Hz. This frequency lies in the regime of input heaving frequencies that yield the largest horizontal velocities relative to the clamped wing. We proceed now with a numerical investigation of the surprising dynamics observed in the experiments.

III. EQUATIONS OF MOTION AND COMPUTATIONAL METHOD

We model the flapping wing by a two-dimensional body of elliptic cross section, illustrated in Fig. 5, having center of mass $\mathbf{x_0}(t)$, pitching angle $\theta(t)$, and major and minor axis lengths $2a$ and $2b$. The wing edge connected to the support bar shown in Fig. 1 is represented here as a single, vertically driven pivot point $y_p(t)$, with amplitude of oscillation A^* and frequency f: $y_p(t)=y_0(t)+a_p\sin(\theta)=A^*\cos(2\pi ft)$, with a_p as the distance from the wing center to the pivot point. The wing motion is described by linear and angular momentum balance,

$$m\ddot{\mathbf{x}}_\mathbf{0} = F_D\hat{\mathbf{y}} + \mathbf{F}_{\text{Fluid}}, \tag{3}$$

$$I_R\ddot{\theta} = -\kappa^*\theta + a_p\cos(\theta)F_D + \tau_{\text{Fluid}}, \tag{4}$$

where m is the wing mass, $I_R=m(a^2+b^2)/4$ is the moment of inertia, F_D is the vertical driving force necessary to keep $y_p(t)$ on a fixed orbit, and $\mathbf{F}_{\text{Fluid}}$ and τ_{Fluid} are the fluid forces and torque, described below. A linear, torsional spring placed at the pivot point introduces a restorative torque, $-\kappa^*\theta$, which acts to return the wing to the horizontal plane, $\theta=0$. The damping of the spring itself is neglected. While other authors considered pivot locations at the quarter chord and one-third chord, here we will match the experiments under consideration by setting $a_p/a=1$.[11,19]

To determine the fluid forces and torque, the wing is coupled to the two-dimensional Newtonian fluid. In so doing, the primary flow relevant to the dynamics is assumed to vary insubstantially along the three-dimensional wingspan. The fluid equations are solved in a frame moving and rotating with the body, $\tilde{\mathbf{x}}=\underline{\mathbf{R}}^{-1}(\mathbf{x}-\mathbf{x_0})$, where $\underline{\mathbf{R}}=\begin{pmatrix}\cos(\theta) & -\sin(\theta)\\ \sin(\theta) & \cos(\theta)\end{pmatrix}$ is a time dependent rotation matrix. The Navier–Stokes equations are written in the vorticity/stream function formulation in the body frame as

$$\tilde{\omega}_t + 2\ddot{\theta} + \tilde{\mathbf{u}}\cdot\nabla\tilde{\omega} = \nu\Delta\tilde{\omega} \quad \text{in } \Omega, \tag{5}$$

$$\Delta\tilde{\psi} = \tilde{\omega} \quad \text{in } \Omega, \tag{6}$$

$$\tilde{\mathbf{u}} = \nabla^{\perp}\tilde{\psi} = (-\tilde{\psi}_{\tilde{y}}, \tilde{\psi}_{\tilde{x}}) \quad \text{in } \Omega, \tag{7}$$

where $\tilde{\mathbf{u}}$ ($\mathbf{u}$) is the fluid velocity in the body (laboratory) frame, μ is the fluid viscosity, ρ is the fluid density, $\omega = v_x - u_y = \tilde{v}_{\tilde{x}} - \tilde{u}_{\tilde{y}} + 2\dot{\theta} = \tilde{\omega} + 2\dot{\theta}$ is the vorticity, and $\tilde{\psi}$ is the stream function for $\tilde{\mathbf{u}}$. Ω is the fluid domain, and we denote the body surface and fluid boundary by $\partial\Omega$. We assume that the fluid velocity and vorticity in the laboratory frame decay rapidly in the far field, and that the body and fluid velocities match on the surface (the no-slip condition),

$$\tilde{\omega}(|\mathbf{x}| \to \infty, t) = -2\dot{\theta}, \tag{8}$$

$$\nabla^{\perp}\tilde{\psi}(|\mathbf{x}| \to \infty, t) \sim -\underline{\mathbf{R}}^{-1}\dot{\mathbf{x}}_{\mathbf{0}} - \dot{\theta}\tilde{\mathbf{x}}^{\perp}, \tag{9}$$

$$\nabla^{\perp}\tilde{\psi}(\mathbf{x} \in \partial D, t) = 0. \tag{10}$$

Recall that $\dot{\mathbf{x}}_{\mathbf{0}}(t)$ is the translational velocity in the *laboratory frame*. The fluid forces and torque on the body are determined by integrating the fluid stress along its surface, $\mathbf{F}_{\text{Fluid}} = \int_{\partial D} \mathbf{T}\hat{\mathbf{n}} ds$ and $\tau_{\text{Fluid}} = \int_{\partial D} \mathbf{x} \times \mathbf{T}\hat{\mathbf{n}} ds$, where $\mathbf{T} = -p\mathbf{I} + \mu(\nabla\mathbf{u} + \nabla\mathbf{u}^T)$ is the fluid stress with p as the fluid pressure, and $\hat{\mathbf{n}}$ is the outward pointing unit normal on the body surface. The initial positions and velocities are $\mathbf{x}_{\mathbf{0}}(0) = (0,0)$, $\dot{\mathbf{x}}_{\mathbf{0}}(0) = \theta(0) = \dot{\theta}(0) = 0$, and the fluid is initially quiescent, $\tilde{\omega}(\mathbf{x}, t=0) = \mathbf{u}(\mathbf{x}, t=0) = 0$.

The system is made dimensionless by scaling on the length $L=a$, the velocity $U=af$, and the time $T=L/U$. Variables defined above are henceforth understood to be normalized by these scales. The system is then controlled by six dimensionless parameters: a frequency Reynolds number $\text{Re}_f = \rho UL/\mu$, a dimensionless flapping amplitude $A = A^*/L$, the aspect ratio $e = b/a$, a dimensionless spring constant $\kappa = \kappa^*/(\rho L^2 U^2)$, and the mass ratio $M = m/(\pi e \rho L^2)$. The body is density matched to the fluid when $M=1$. Another important dimensionless quantity is the phase difference between heaving and pitching, ϕ, introduced in the previous section.

Equations (5)–(10) are solved in a body-conforming coordinate system, an approach that has seen previous application.[13,20–22] Namely, the system is transformed into elliptic-cylindrical coordinates (ξ, η) in the frame moving with the body:

$$\tilde{x} + i\tilde{y} = (1 - e^2)^{1/2}\cosh(g(\xi) + i\eta)$$
$$\xi \in [0, \infty), \quad \eta \in [0, 2\pi), \tag{11}$$

where $g(\xi) = g_0 + (g_B - g_0)\xi$, with g_0 and g_B defined so that the coordinates $\xi=0$ and $\xi=1$ describe the body surface and outer computational boundary, respectively. A small portion of the computational grid is shown in Fig. 6 for an aspect ratio $e=0.1$. A uniform discretization in ξ places an increased density of physical mesh points near the body surface in this coordinate system, where the vorticity and its derivatives are most important to the dynamics.

The nondimensionalized equations in the new coordinate system are

$$\tilde{\omega}_t + 2\ddot{\theta} + \frac{1}{J}\nabla^{\perp}\tilde{\psi} \cdot \nabla\tilde{\omega} = \frac{1}{Jg_{\xi}\,\text{Re}_f}(\tilde{\omega}_{\xi\xi} + g_{\xi}^2\tilde{\omega}_{\eta\eta}), \tag{12}$$

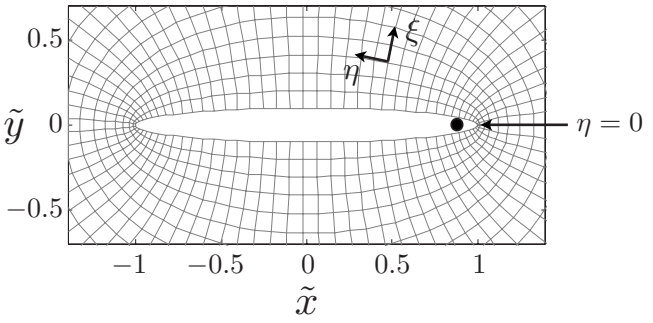

FIG. 6. The elliptic-cylindrical, body-conforming coordinate system for a wing with aspect ratio $e=0.1$.

$$\tilde{\psi}_{\xi\xi} + g_{\xi}^2\tilde{\psi}_{\eta\eta} = Jg_{\xi}\tilde{\omega}, \tag{13}$$

where the Jacobian $J = \tilde{x}_{\xi}\tilde{y}_{\eta} - \tilde{x}_{\eta}\tilde{y}_{\xi}$ is a local scaling factor, and $g_{\xi} = g_B - g_0$. The boundary conditions become

$$\tilde{\omega}(\xi \to \infty, \eta, t) = -2\dot{\theta}, \tag{14}$$

$$\tilde{\psi}_{\xi}(\xi \to \infty, \eta, t) \sim -\frac{\dot{\theta}}{2}\partial_{\xi}(\tilde{x}^2 + \tilde{y}^2) - \tilde{\mathbf{x}}_{\xi}^{\perp} \cdot \underline{\mathbf{R}}^{-1}\dot{\mathbf{x}}_{\mathbf{0}}, \tag{15}$$

$$\tilde{\psi}(0, \eta, t) = 0, \quad \tilde{\psi}_{\xi}(0, \eta, t) = 0. \tag{16}$$

A free integration constant in the description of ψ may be set to zero by a simple redefinition, since the stream function only enters the dynamics by its derivatives (with the single exception at the body surface).

A convenient representation of the body acceleration is achieved by a manipulation of the velocity/pressure form of the Navier–Stokes equations. The translational body acceleration is rewritten in the laboratory frame as

$$(M\pi e)\ddot{\mathbf{x}}_{\mathbf{0}} = F_D\hat{\mathbf{y}} + \mathbf{F}_{\text{Fluid}}, \tag{17}$$

$$\frac{M\pi e(1+e^2)}{4}\ddot{\theta} = -\kappa\theta + \cos(\theta)F_D + \tau_{\text{Fluid}}, \tag{18}$$

and the fluid forces and torque are written as integrations against the vorticity and its normal derivative on the body surface,

$$\mathbf{F}_{\text{Fluid}} = \pi e\ddot{\mathbf{x}}_{\mathbf{0}} + \frac{1}{\text{Re}_f}\underline{\mathbf{R}}\int_0^{2\pi}\left(-\tilde{\mathbf{x}}^{\perp}\frac{\tilde{\omega}_{\xi}}{g_{\xi}} + \tilde{\mathbf{x}}_{\eta}\tilde{\omega}\right)\Bigg|_{\xi=0} d\eta, \tag{19}$$

$$\tau_{\text{Fluid}} = \frac{\pi e(1+e^2)}{2}\ddot{\theta} + \frac{1}{\text{Re}_f}\int_0^{2\pi}\left(-\frac{1}{2}|\tilde{\mathbf{x}}|^2\frac{\tilde{\omega}_{\xi}}{g_{\xi}} + e(\tilde{\omega} + 2\dot{\theta})\right)\Bigg|_{\xi=0} d\eta. \tag{20}$$

The dimensionless heaving force F_D is determined algebraically by twice differentiating the geometric relationship $y_p(t) = y_0(t) + \sin(\theta)$ and using Eqs. (17) and (18) (see Appendix A); the dimensionless heaving displacement is simply

$y_p(t)=A\cos(2\pi t)$. Finally, we define the angle of attack $\alpha(t)$ as that measured between the wing's major axis and the instantaneous direction of motion, as illustrated in Fig. 5,

$$\alpha(t)=\tan^{-1}\left(\frac{\dot{x}_0\tan(\theta)-\dot{y}_0}{\dot{y}_0\tan(\theta)+\dot{x}_0}\right). \tag{21}$$

A. Method of solution

A mixed Fourier/finite-differences discretization is applied to the fluid equations. The computational grid is generated by uniform discretizations of ξ and η using $N_1\times N_2$ points: grid points are located at $(\xi_i,\eta_j)=(i\Delta\xi,j\Delta\eta)$, where $(\Delta\xi,\Delta\eta)=(1/(N_1-1),2\pi/N_2)$. Derivatives in ξ are computed using fourth-order difference formulae; derivatives in η are computed with spectral accuracy in Fourier space. Asymmetric difference formulae are used to compute radial derivatives at grid points near the inner and outer boundaries. In practice the accuracy achieved in simulations is between third- and fourth-order. A second-order, implicit Crank–Nicholson scheme is used for time stepping on the linear terms, and second-order Adams–Bashforth for the advection term. Convergence and other tests of the simulations are presented as Appendix B.

The boundary conditions are treated implicitly, so that the boundary values of $\tilde{\omega}$ on the surface and $\tilde{\psi}$ in the far-field are part of the linear system to be solved; explicit treatment of the boundary conditions leads to a constrictive Courant–Friedrichs–Lewy condition for stability.[20] The vorticity $\omega=\tilde{\omega}+2\dot{\theta}$ is set to zero on the outer boundary at $\xi=1$, which is chosen at a distance far enough from the body to ensure that the vorticity does not approach this boundary for the duration of computation. Increased accuracy may be achieved by accounting for the error made in applying this boundary condition, as shown in Ref. 23. However, in a similar study, this correction was not found to alter significantly the computational results, and so we neglect it.[24] Finally, we use the two stated boundary conditions for ψ on the body surface to generate a numerical boundary condition for the vorticity there. A trivial modification of Briley's method is used to generate a numerical boundary condition for the vorticity (see Refs. 22, 25, and 26).

A generalized minimum residual (GMRES) iterative scheme[27] was constructed to solve the large linear system to a small error tolerance (10^{-7}). Further decreasing this inversion tolerance did not alter the simulation results, so the numerical errors are due to discretization only. While Gaussian elimination requires $O(N^3)$ flops to invert an $N\times N$ matrix, GMRES requires only $O(N^2p)$ flops where p is the number of iterative steps, a vast savings for large, well-conditioned matrices. The iterations converge to within the specified tolerance in approximately 20–200 iterations. Preconditioning is achieved by solving the following nearby linear system which only includes the highest derivatives (the stiffest terms) at each time step $t=t^{n+1}$, given a known right hand side **b** (see Ref. 24):

$$\left(1-\frac{\Delta t}{2\,\mathrm{Re}_f}\Delta\right)\tilde{\omega}^{n+1}=b_1(\xi,\eta),\quad \text{in } \Omega, \tag{22}$$

$$\Delta\tilde{\psi}^{n+1}-\tilde{\omega}^{n+1}=b_2(\xi,\eta)\quad \text{in } \Omega, \tag{23}$$

where $\tilde{\omega}^{n+1}=\tilde{\omega}(\mathbf{x},t^{n+1})$. The preconditioning problem decouples the equations for $\tilde{\omega}$ and $\tilde{\psi}$, which are then amenable to fast inversion algorithms for banded systems and are solved sequentially.

To linearize the time-stepping operator, and also to accelerate the convergence of the iterative solver, the pitching angle θ^{n+1} is approximated to second order from information at previous timesteps: $\bar{\theta}^{n+1}=\theta^{n-1}+2\Delta t\dot{\theta}^n$. The body acceleration equations are also discretized, and the linear system to be solved at each time step includes the equations for the velocities at the $(n+1)^{\text{th}}$ time step [from Eqs. (17)–(20)],

$$\frac{(M-1)\pi e}{\Delta t}\left(\frac{3}{2}\dot{x}_0^{n+1}-2\dot{x}_0^n+\frac{1}{2}\dot{x}_0^{n-1}\right)=F_x^{n+1}, \tag{24}$$

$$\dot{y}_0^{n+1}+\cos(\bar{\theta}^{n+1})\dot{\theta}^{n+1}=\dot{y}_p^{n+1}, \tag{25}$$

$$\frac{(M-2)I}{\Delta t}\left(\frac{3}{2}\dot{\theta}^{n+1}-2\dot{\theta}^n+\frac{1}{2}\dot{\theta}^{n-1}\right)$$
$$=-\kappa\tilde{\theta}^{n+1}+\cos(\bar{\theta}^{n+1})F_D^{n+1}+T^{n+1}, \tag{26}$$

where

$$F_x=\frac{1}{\mathrm{Re}_f}\hat{\mathbf{x}}\cdot\underline{\mathbf{R}}\int_0^{2\pi}\left(-\tilde{\mathbf{x}}^{\perp}\frac{\tilde{\omega}_\xi}{g_\xi}+\tilde{\mathbf{x}}_\eta\tilde{\omega}\right)\Big|_{\xi=0}d\eta, \tag{27}$$

$$T=\frac{1}{\mathrm{Re}_f}\int_0^{2\pi}\left(-\frac{1}{2}|\tilde{\mathbf{x}}|^2\frac{\tilde{\omega}_\xi}{g_\xi}+e(\tilde{\omega}+2\dot{\theta})\right)\Big|_{\xi=0}d\eta, \tag{28}$$

$$I=\frac{\pi e(1+e^2)}{4}. \tag{29}$$

In order to retain the formal accuracy of the numerical method, the initial driving force at $t=0$ is mollified in the following fashion. The numerical pivot displacement imposed is $\tilde{y}_p(t)=y_p(t)[t^4/(1+t^4)]$, so that the initial velocities are introduced as $O(t^4)$, and $|y_p(t)-\tilde{y}_p(t)|<.01|y_p(t)|$ for $t>3.2$, with rapid convergence to the desired periodic displacement $y_p(t)$ thereafter.

IV. FIVE REGIMES OF FLAPPING LOCOMOTION

We begin by presenting the dynamics for a particular numerical simulation which illustrates various generic features seen over a wide range of the parameter space. For the remainder of this work we consider only the flapping amplitude $A=1/2$. Figure 7 shows the vorticity generated by the pitching wing during the early stages of the flapping motion, with Reynolds number $\mathrm{Re}_f=15$, mass $M=1.01$, spring constant $\kappa=50\,000$, and aspect ratio $e=0.1$. Vorticity contours are shown at values $\omega=\pm 2^p$ for $p=0,1,\ldots,7$ with dashed lines indicating negative values. At $t=0.75$ the pivot point (on the wing's rightmost edge) is moving upward, and the body is rotating in the counterclockwise direction. Associated with this rotation is the development of negative vorticity in the boundary layers near the left and right wing edges, where the wing geometry varies most dramatically. The mo-

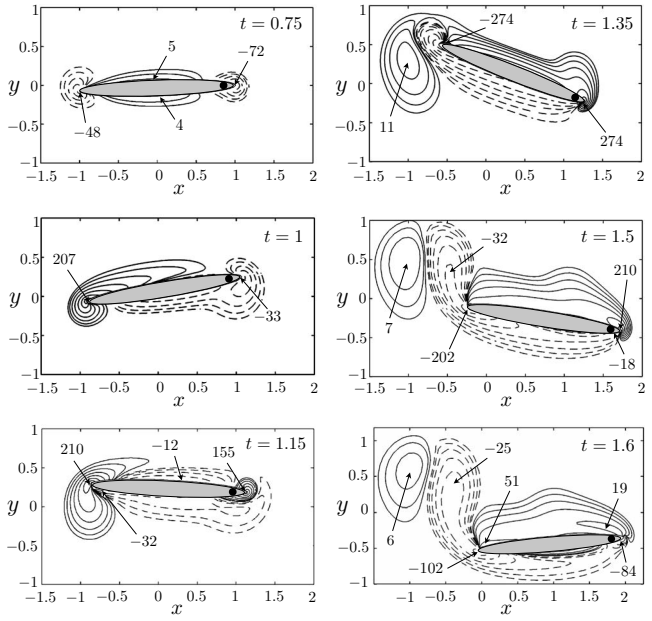

FIG. 7. Development of the first large scale vortical structure and the onset of horizontal motion. The previous LEV drifts backward relative to the body and re-enforces the newly formed TEV. Vorticity contours are shown at values $\omega = \pm 2^p$ for $p = 0, 1, \ldots, 7$ with dashed lines indicating negative values; other extremal values of vorticity are also indicated.

tion is not a pure rotation; the center of mass is also moving upward, and accordingly the vorticity on the right is larger in magnitude than the vorticity on the left. At $t=1$ the pivot point has zero vertical velocity and the local vorticity there has significantly decayed. However, during the upstroke the body has deflected out of the horizontal plane due to inertia and fluid forces, and the torsional spring imparts a torque at the pivot point. As a result, the leftmost wing edge continues to move upward. By $t=1.15$ the wing has crossed the horizontal plane, and, as the driving pivot begins its downward plunge, the body continues to rotate in the clockwise direction. The wing motion is generating positive vorticity in the boundary layers near both edges, but since the body is still rotating clockwise due to the torsional spring response and inertia, the vorticity is now larger on the left edge than on the right.

The body continues to rotate due to the inertia of both the body and surrounding fluid, and by $t=1.35$ the left edge has reached its apex with a larger vertical displacement than the maximal pivot displacement. Once again the restorative torque acts to return the body to the horizontal plane, and the left edge begins to move downward. Corresponding to this direction change, large negative vorticity accumulates near the left edge, and the positive vorticity that was generated on the upstroke is disconnected (shed) from the body surface. The transition to vortex detachment in the intermediate regime of $\mathrm{Re}_f=1$ to $\mathrm{Re}_f=100$ has been studied by Miller and Peskin.[28] For $t \in (1.5, 1.6)$ the body undergoes its restorative rotation; associated with the vortical shedding on the left is a fluid force on the body surface [via Eqs. (19) and (20)] and the wing moves to the right. Meanwhile, the positive vorticity created near the pivot edge during $t \in (1, 1.5)$ has drifted back along the upper body surface and has accumulated toward the leftmost edge, as the body prepares to shed the large negative vorticity and begin the cycle anew.

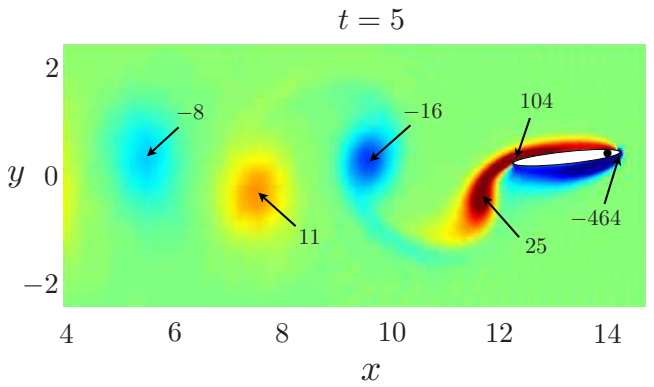

FIG. 8. (Color online) Vorticity profile at $t=5$, with mass $M=1.01$, frequency Reynolds number $\mathrm{Re}_f=15$, spring constant $\kappa=50\,000$, flapping amplitude $A=1/2$, and aspect ratio $e=0.1$. The wake structure is known as a reverse von-Kármán vortex street, corresponding to forward thrust.

Figure 8 shows the vortical wake at the beginning of the fifth flapping cycle. As the wing is driven vertically through the fluid, concentrated vorticity is shed periodically from the trailing edge. The vertical separation between positive and negative vortices in the wake coincides with a jet of fluid moving in the direction opposite the body motion, indicative of thrust. This particular vortical structure is the reverse von-Kármán vortex street mentioned previously, and has been the subject of many experiments and simulations.[12,29–31] This structure contrasts with the classical von-Kármán vortex street observed behind bluff bodies, where the vorticity is oppositely signed and corresponds instead to drag.[32]

In the present example the body moves to the right (forward free flight) with a regular, periodic motion. Figure 9(a) shows the horizontal and angular velocities as functions of time. The body reaches a periodic steady-state in approximately four to six flapping periods, though the velocities

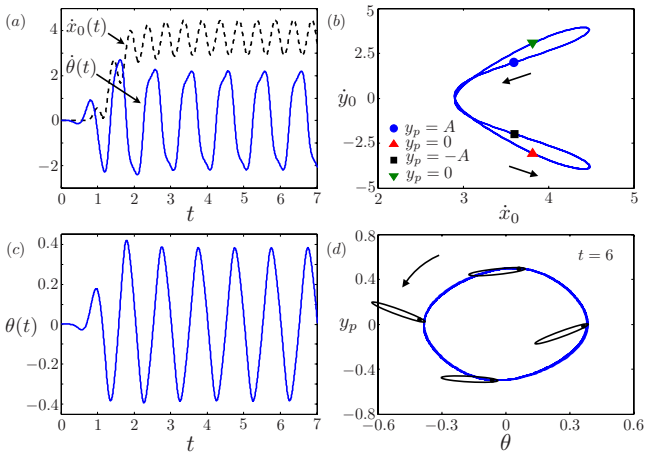

FIG. 9. (Color online) (a) Horizontal velocity $\dot{x}_0(t)$ and angular velocity $\dot{\theta}(t)$ corresponding to the flapping body shown in Fig. 8. (b) Phase diagram relating the horizontal and vertical centroid velocities, $\dot{x}_0(t)$ and $\dot{y}_0(t)$. An arrow indicates the direction of increasing time. (c) Time series of the pitching angle $\theta(t)$. (d) Phase diagram relating the pitching angle $\theta(t)$ and the vertical pivot displacement $y_p(t)$. Body orientations are included for times corresponding to the marked points in (b).

during the first two flapping periods are strongly affected by the ramped form of the pivot displacement $y_p(t)$. The horizontal velocity is unsteady but periodic, varying within a band of nearly 22% of its mean. Figure 9(b) shows a phase diagram relating the centroid's horizontal and vertical velocities once the periodic steady state has been reached, along with markers indicating the vertical pivot displacement. The horizontal and vertical velocities are largest almost simultaneously, occurring after the pivot has crossed the x-axis on an upward or downward plunge, but before it has reached its apex. Figures 9(c) and 9(d) show the pitching angle $\theta(t)$ and a phase diagram relating $\theta(t)$ to the vertical pivot displacement $y_p(t)$. The pitching angle undergoes sawtoothlike oscillatory dynamics, and the body experiences its largest angular displacement during the early, ramping stage of the flapping motion. This large, early angular deflection was also observed in the experiments. Vorticity is shed from the body on each flapping half period and each such event drives the horizontal motion equally in this case.

The Strouhal number is a nondimensionalized frequency, defined here as $\mathrm{St}=2A^*f/U_s$, where U_s is the average dimensional swimming speed. This dimensionless number can be used to characterize vortical shedding and hence the wake structure.[1] Having scaled velocities on af, and with $A^*/a=1/2$, the Strouhal number reported here is $\mathrm{St}=1/\langle\dot{x}_0\rangle$. In this first example we find $\mathrm{St}=0.26$. Experiments have shown in a similar system that thrust development is hydrodynamically optimal for $0.25<\mathrm{St}<0.40$.[9,33] Most fish and cetaceans have been observed to locomote in this range of Strouhal numbers.[1,33,34]

The experiments were designed with the flapping frequency f as a variable control parameter. Having scaled the velocities on this frequency, f enters the dynamics not only through the body and fluid velocities, but also through the frequency Reynolds number $\mathrm{Re}_f\sim f$ and the spring constant $\kappa\sim f^{-2}$. In order to better relate the simulations to the experimental work, we begin by scanning the available parameter space along this particular path of increasing f.

Figure 10(a) shows the mean horizontal velocity over a range of flapping frequencies f for aspect ratio $e=0.1$ and mass ratio $M=10$, where $\mathrm{Re}_f=10f$ and $\kappa=1000/f^2$. f is now understood to be dimensionless though scaling the Reynolds number and spring constant like the heaving frequency, and will be referred to as such. The body is initially at rest for these simulations with one exception which will be discussed later in more detail. Mean velocities are computed once the cycle-averaged velocities are within 1% of their final values in the periodic steady state.

We note the strong qualitative agreement between the simulation results in Fig. 10 and the experimental results in Fig. 2 even though the Reynolds numbers reached in the experiments were significantly larger ($\mathrm{Re}_f\approx 10^5$). We include simulation results for a flapping clamped wing, as in the studies of Refs. 12 and 13. The clamped wing simulations show approximately linear growth in Re_f, which agrees generally with the previous experimental and numerical work; the simulations of Ref. 13 use a larger flapping amplitude, $A=1$, so we do not expect exact agreement. Figure 10 indicates four well separated dynamical regimes in the heaving

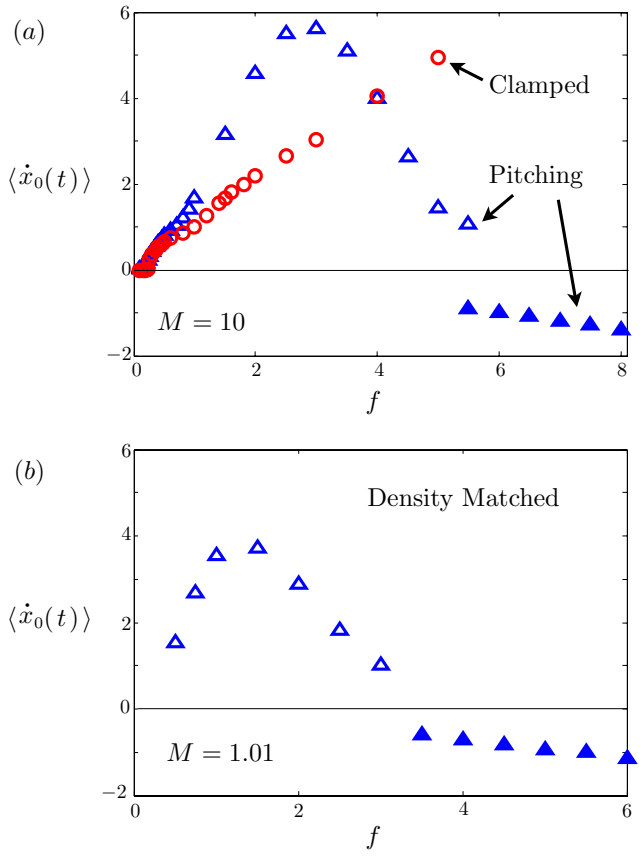

FIG. 10. (Color online) (a) Mean horizontal velocities of a flapping, pitching wing with frequency Reynolds number $\mathrm{Re}_f=10f$, spring constant $\kappa=1000/f^2$, flapping amplitude $A=1/2$, aspect ratio $e=0.1$, and mass ratio $M=10$. Results for a clamped wing (nonpitching, $\kappa=\infty$) are included for comparison. Passive pitching leads to five regimes of motion; the first four are shown here. (b) The (nearly) density matched case, $M=1.01$. A density matched clamped plate exhibits chaotic dynamics in this regime, so no averaged velocity is shown.

frequency: a first regime of nearly symmetric fluid flow, a second regime of improved performance when compared with the clamped wing, a third regime of relative underperformance, and a fourth regime of direction reversal and, for a heavier body ($M=10$), bistability. A fifth regime for extremely large flapping frequencies will also be considered.

Similar data for a nearly density matched case, $M=1.01$, are shown in Fig. 10(b). The trends are similar to those seen in the heavier wing dynamics ($M=10$), with the one exception that we do not detect any flapping frequencies corresponding to bistability in the density matched case. Hence, we suggest that inertia may play an important role in determining the nature of this particular transition. A closer examination of this transition, which is not presently understood, will be the topic of a future work. Of particular note here is the achievement of periodic steady state dynamics for a density matched pitching body. A flapping clamped (nonpitching) wing in this regime of Reynolds number has been shown to exhibit chaotic dynamics;[13] hence we have not included any averaged data for a clamped wing in Fig. 10(b). While elasticity is known in some physical systems to introduce instabilities and irregularities such as buckling, for flapping locomotion we find that it is possible for an

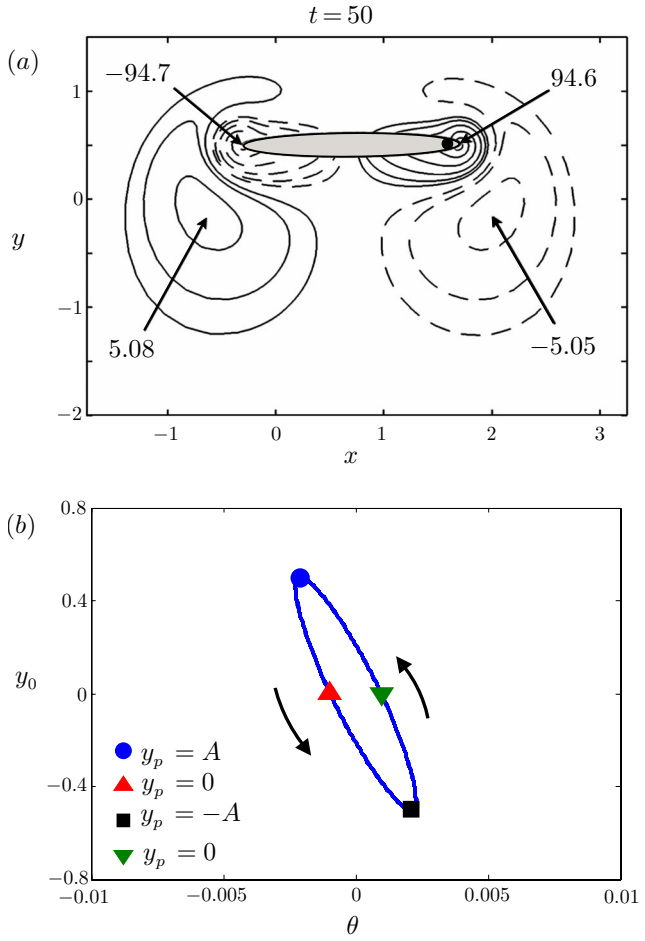

FIG. 11. (Color online) (a) The vorticity contours generated by the pitching wing for flapping frequency $f=0.2$ ($\mathrm{Re}_f=2$, $\kappa=25\,000$). The fluid flow generated by the passively pitching wing is very nearly (but not exactly) left/right symmetric. Contour values are the same as in Fig. 7. (b) A phase diagram relating the pitching angle θ to the vertical displacement y_0. Arrows indicate the direction of increasing time.

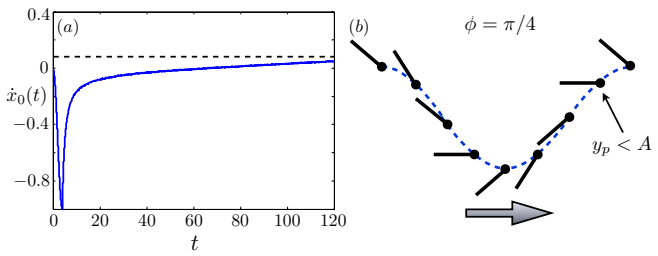

FIG. 12. (Color online) (a) The horizontal velocity for frequency Reynolds number $\mathrm{Re}_f=2$ for the pitching wing shown in Fig. 11. The body is seeded initially with a negative velocity during $t \in (0,5)$, but once the body is free to move horizontally the dynamics return to the forward moving periodic state. (b) Kinematics for a heaving/pitching phase difference $\phi=\pi/4$.

elastic response to *suppress* chaotic or otherwise irregular dynamics.

We proceed now to discuss the five regimes of flapping wing dynamics. In the following section we fix the mass ratio $M=10$ and aspect ratio $e=0.1$. The heavier body and thin wing profile are selected to eliminate the more complicated, unsteady dynamics mentioned above.

A. Continuous departure from the Stokesian regime

We begin our investigation with a discussion on the development of forward motion from very small flapping frequencies. In this first regime of flapping wing dynamics, the frequency Reynolds number is very small and the relative spring stiffness is very large. Figure 11(a) shows the vorticity contours generated by a pitching wing in this regime with flapping frequency $f=0.2$ ($\mathrm{Re}_f=2$, $\kappa=25\,000$) at a time when the pivot edge has reached its apex, ($y_p(t=50)=A$). The fluid flow generated by the passively pitching wing is very nearly (but not exactly) left/right symmetric. The vorticity on the body at the trailing (left) edge has a minimum of -94.7, while the vorticity at the leading (right) edge is slightly smaller in magnitude, with a maximum of 94.6. A corresponding horizontal force on the wing [via Eqs. (19) and (20)] drives the wing slowly to the right in a forward moving state, with $\langle \dot{x}_0 \rangle \approx 0.04$.

Figure 11(b) shows a phase diagram of the pitching angle θ and the vertical pivot displacement y_p. The maximum pitching angle in the periodic steady state is $\theta_{\max}=.0023$, and the heaving/pitching phase difference is $\phi=0.5186<\pi/4$. Thus, the pitching leads the heaving, and the body begins to reverse its direction of rotation before the end of the heaving cycle [see Fig. 12(b)]. Unlike in the clamped wing experiments ($\kappa=\infty$), where the body can move in either direction with a sensitive dependence upon initial conditions, here we find that the asymmetry due to pitching sends the body unidirectionally toward the right for forward flapping flight. To investigate the stability of the forward moving state in the pitching wing system, we ramp a body flapping with frequency Reynolds number $\mathrm{Re}_f=2$ to a negative initial velocity, $\dot{x}_0(t=0.5)=-1$. Figure 12 shows the horizontal velocity of the body in the first 120 heaving periods. Once released, the wing slows to within 10% of its initially seeded velocity within approximately 15 flapping periods, and then very slowly moves into the forward moving state. By the end of the first 120 periods, the body has not yet reached its final steady state mean velocity of $\langle \dot{x}_0 \rangle \approx 0.04$, as determined in the previous simulation where the body is initially at rest.

The mean horizontal velocities in the first regime of flapping frequency ($f<1$) for both pitching and clamped (nonpitching) wings are shown in Fig. 13 on linear and logarithmic scales. The clamped wing is seeded with a small positive initial velocity to ensure a final motion to the right (if nonzero). For very small heaving frequencies, the asymmetry from pitching leads to the development of forward flapping locomotion. In contrast, below a critical frequency Reynolds number, the clamped body settles to zero horizontal velocity, as shown in previous experiments[12] and simulations.[13] Thus, by the introduction of a slight flexibility, the departure from the Stokesian regime ($\mathrm{Re}_f \ll 1$) appears to be continuous. At $f \approx 1/3$, the velocity transitions to approximately linear growth in the flapping frequency f. In this regime, the velocity of the clamped wing is everywhere bounded above by the velocity of the pitching wing.

A heaving clamped wing with no pitching undergoes a time-reversible motion and cannot locomote in a Stokesian

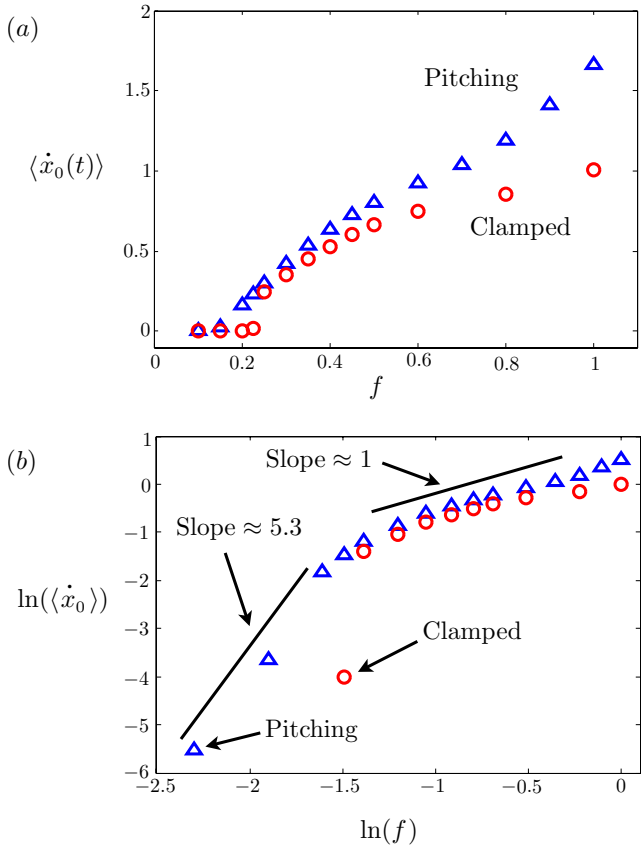

FIG. 13. (Color online) (a) Dependence of mean horizontal velocity on the flapping frequency in the first regime of locomotion, with frequency Reynolds number $\mathrm{Re}_f = 10f$, spring constant $\kappa = 1000/f^2$, and mass ratio $M = 10$. (b) The same, on a logarithmic scale.

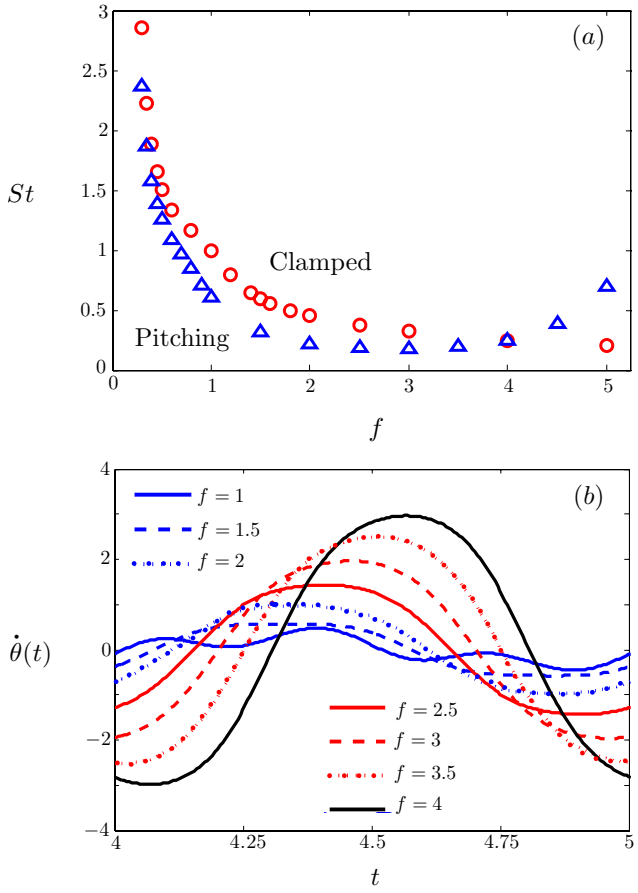

FIG. 14. (Color online) (a) The Strouhal number is minimal at $f = 3$ with a value of St = 0.178, while St = 0.329 for the analogous nonpitching wing, an 85% decrease. (b) Angular velocity profiles for a selection of flapping frequencies f are shown. The minimal Strouhal number here corresponds with an approximately sinusoidal pitching profile and a heaving/pitching phase difference $\phi \approx \pi/2$.

fluid ($\mathrm{Re}_f = 0$), a result known as the Scallop theorem.[35] Other types of flapping motions have been considered by Lauga,[36] who shows that some reversible motions involving large oscillation amplitudes also yield a continuous departure from the Stokesian limit. A transition in vortex shedding for Reynolds numbers $\mathrm{Re}_f \approx 32$ was shown by Miller and Peskin.[28]

B. Flexibility yields improved performance

In the second regime of flapping locomotion ($f \approx 1-3$) the pitching wing continues to outperform the clamped wing, but with larger differences in horizontal velocity (see Fig. 10). In addition, the fluid motion in this regime is no longer nearly left/right symmetric as in the first regime and a thrust wake develops behind the forward moving body. The dependence of the Strouhal number on the flapping frequency f is shown in Fig. 14(a). The pitching wing takes on a maximum mean horizontal velocity of $\langle \dot{x}_0 \rangle = 5.6$ at approximately $f = 3$ ($\mathrm{Re}_f = 30$, $\kappa = 111$), corresponding to a Strouhal number of approximately 0.178. In contrast, the Strouhal number for the corresponding clamped wing is St = 0.329. The pitching wing moves horizontally with smaller Strouhal numbers up to $f \approx 4$, at which point the pitching and clamped wings move at approximately the same speed. Figure 14(b) shows the angular velocity profiles over one flapping cycle for a selection of flapping frequencies. The minimal Strouhal number found here corresponds to an approximately sinusoidal pitching profile with heaving/pitching phase difference $\phi \approx \pi/2$. This finding is discussed in greater detail below. The previously defined natural resonant frequency is found for this parameter path to correspond to the dimensionless frequency $f \approx 3.5$. The horizontal velocity therefore reaches its peak, as in the experiments, when the flapping frequency is near the immersed system's resonant frequency.

We consider the changes in the fluid-body interactions in this second regime of motion leading to the improved performance of the pitching wing. Figure 15 shows the vorticity generated at two different flapping frequencies during the pivot's downward plunging motion. The first row of images shows the dynamics for flapping at frequency $f = 1$ ($\mathrm{Re}_f = 10$, $\kappa = 1000$, $\langle \dot{x}_0 \rangle = 1.7$). As the body is driven downward, vorticity is created as fluid passes around both the leading and trailing edges. The vorticity rapidly separates away from the body, similar to the dynamics seen in the wake behind a flat plate held in an oncoming flow.[32] However, the body pitches due to the fluid forces acting on it, and increased thrust is generated by the trailing edge when the torsional spring restores the body toward the horizontal plane. The combination of the pitching and the restorative

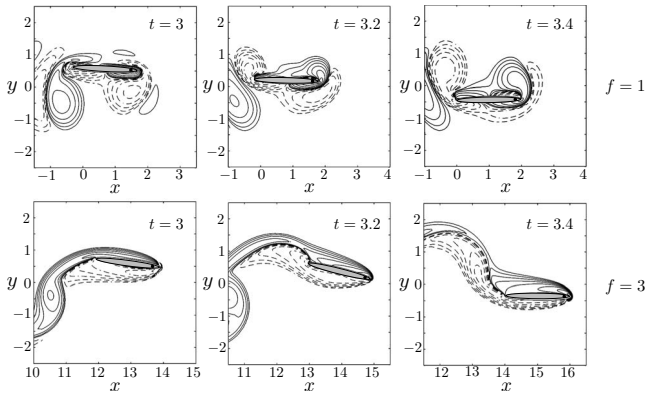

FIG. 15. The vorticity near the body surface at two flapping frequencies $f=1$ and $f=3$ during one heaving half period. The larger flapping frequency corresponds to a smaller relative spring strength, and hence a larger maximum pitching angle. The leading edge vorticity stays closer to the body and re-enforces the trailing edge vorticity, enhancing the thrust production. Contour values are the same as in Fig. 7.

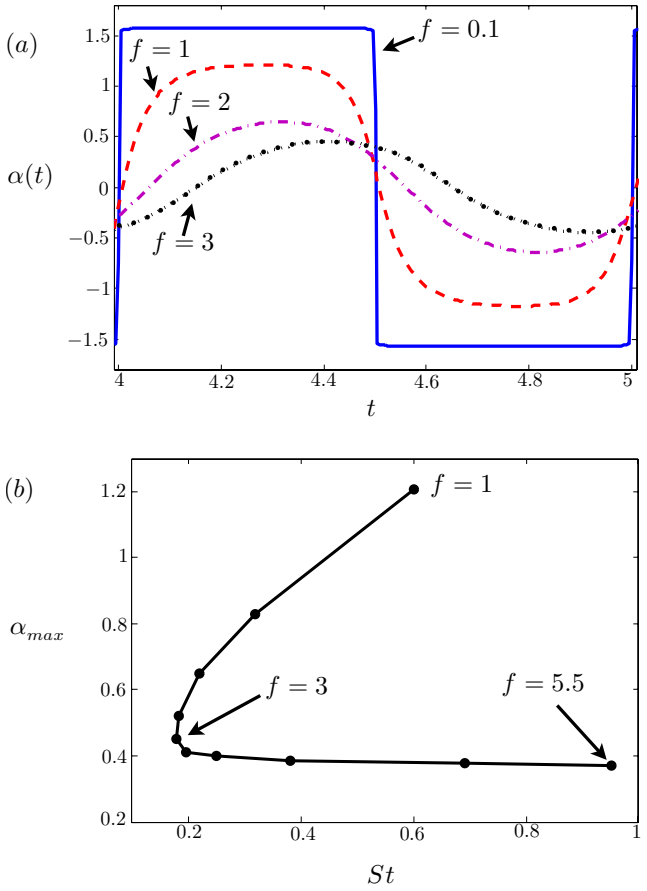

FIG. 16. (Color online) (a) Attack angle profiles $\alpha(t)$ for a selection of flapping frequencies, in radians. (b) Relationship between the maximum attack angle [as in (a)] and the Strouhal number for flapping frequencies $f=1$ to $f=5.5$.

torque leads to stronger vorticity production on the left, and a net fluid force to the right in the direction of the motion.

The second row of images shows the dynamics for a larger flapping frequency ($f=3$, $\mathrm{Re}_f=30$, $\kappa=111$, $\langle \dot{x}_0 \rangle = 5.6$), where the mean horizontal velocity is significantly larger. In contrast with the dynamics in the previous case, as the body is driven downward the relative strength of the torsional spring is much weaker and the body pitches more dramatically. During the stroke the leading edge vorticity does not noticeably separate from the body and passes back along the surface, joining with the trailing edge vorticity of like sign. This vortical re-enforcement increases the strength of the vortex that is shed from the trailing edge (at $t=3.4$), increasing the strength of the leftward moving fluid momentum jet and increasing the body thrust. After the wing deflection allows the leading edge vortex (LEV) to pass to the left, the torsional spring begins to rotate the body back toward the horizontal plane. This final rotation further enhances vorticity production at the trailing edge and ensures a vortical separation. The production and passage of LEVs to the trailing edge and their relationships to thrust and lift are explored by Wang.[6]

The comparison in Fig. 15 confirms the common understanding that the angle of attack is an important means of characterizing the dynamics of a flapping wing. We denote the maximum angle of attack $\alpha_{\max}$ as the maximal attack angle during the periodic steady state motion. The attack angle profiles for simulations with $f \in [0.1, 3]$ are shown in Fig. 16(a). As we have seen in Fig. 15, the angle of attack dictates how LEVs pass backward to re-enforce trailing edge vortices (TEVs) during the heaving period. The larger attack angles for the relatively stiffer flapping wings correspond with significant LEV detachment in this regime. Figure 16(a) shows that the angle of attack becomes more sinusoidal with increasing f, as the mean horizontal velocity increases. The angle of attack at frequency $f=3$ is maximal after the heaving velocity has begun to slow on the downstroke, as indicated in Fig. 15. There, the very small attack angle at $t=3.2$ near the maximum heaving velocity allows for a clean passage of LEV to TEV. Subsequently, toward the end of the downward pivot plunge the body rotation increases the angle of attack, further strengthening the vorticity as it separates from the body. Figure 16(b) shows the maximum pitching angle plotted against the Strouhal number for frequencies $f=1$ to $f=5.5$. The smallest Strouhal number achieved coincides in this case with a maximum pitching angle of approximately 0.45 rad or 26°. The maximal attack angle decays steadily for frequencies increasing from $f=1$ to $f=3$, and then remains nearly constant for the frequencies yielding forward motion. Two periodic steady states along this curve are observed to correspond to the same Strouhal number (or horizontal velocity) between $f=1$ and $f \approx 5$. The above results agree with previous work by Triantafyllou *et al.*,[33] where the lowest Strouhal numbers were found to correspond to sinusoidal attack angles and $\alpha(t)$ was found to be maximal at the largest heaving velocities. Unlike in the kinematic prescription of the above referenced work, here the results are found as a consequence of a dynamic interaction of the fluid and restoring forces.

In Fig. 17 we compare the attack angle profile between pitching and nonpitching wings at flapping frequency $f=2$. The flexibility of the former decreases its maximum attack angle, not unlike the comparison in Fig. 15. The flexibility also induces a phase shift between the heaving position and

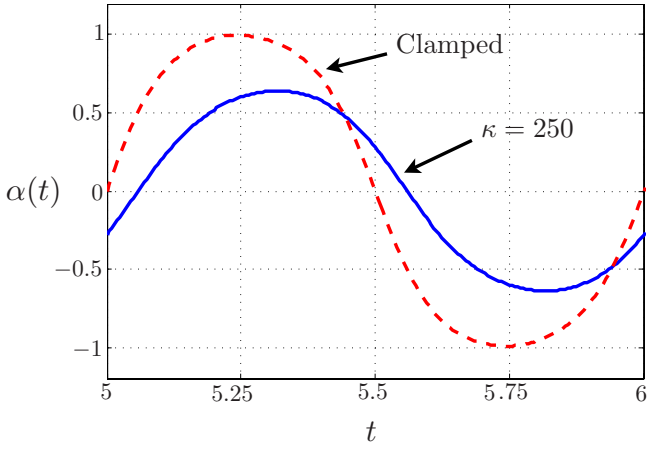

FIG. 17. (Color online) Attack angle comparison between a pitching and a clamped wing. The flexibility in the former decreases the maximum attack angle and induces a phase shift.

the attack angle. The larger attack angles for the clamped plate are associated with the body presenting more surface area to the apparent fluid flow, and thus more significant LEV detachment, as previously discussed.

C. Underperformance, direction reversal, and bistability

As revealed by the experiments, for large enough flapping frequencies, the pitching ceases to aid in the development of horizontal thrust and the dynamics enter a third regime of locomotion characterized by significant underperformance when compared to a clamped (nonpitching) wing. For even larger flapping frequencies f, we find that the flapping dynamics enter into a backward moving periodic state which we consider a fourth regime of coherent locomotion.

Figure 18 shows the dependence of the heaving/pitching phase difference ϕ upon the flapping frequency f. The phase difference decreases for $f \in [0,0.9]$, at which point it takes on its minimum, and then increases monotonically for

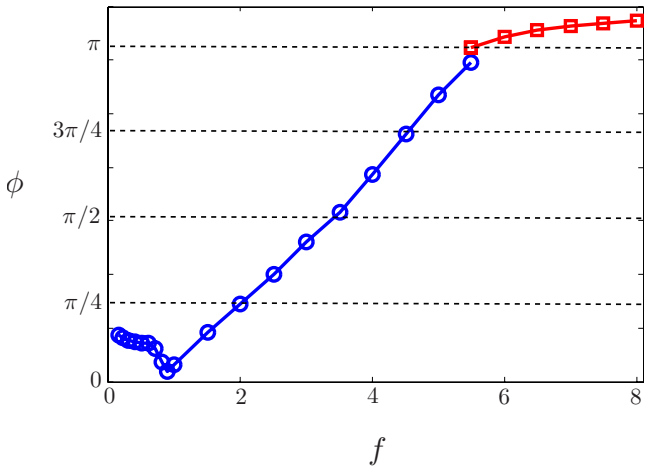

FIG. 18. (Color online) Dependence of the heaving/pitching phase difference ϕ on the flapping frequency f. The circles correspond to forward moving states, the squares to backward moving states.

$f > 0.9$ in the parameter space considered in simulations. The improved horizontal velocities for the pitching wing in the second regime correspond to heaving/pitching phase differences from approximately $\phi \approx 0.5$ to $\phi \approx 1.6$, with a maximum velocity achieved at $f=3$ when $\phi=1.3$. As illustrated in Fig. 3(c), a phase difference $\phi \approx \pi/2$ corresponds to motion such that the trailing edge experiences its greatest displacements and vertical velocities. It confirms intuition then to find larger mean horizontal velocities for nearby phase differences.

As the flapping frequency continues to increase beyond $f=4$, the phase difference continues to increase well beyond $\phi=\pi/2$, and the heaving leads the pitching. Eventually, for $\phi=\pi$, the heaving and pitching are exactly out-of-phase, so that the vertical pivot velocity and angular velocity visit their extrema and zeroes simultaneously. We find that the phase difference $\phi=\pi$ corresponds here to rotational motions with a very small vertical component of velocity ($\dot{y}_0(t)=0$). Both the leading and trailing edges in this case experience approximately the same maximal vertical displacement, that of the driving pivot. We will return to this figure shortly.

A fourth regime of dynamics occurs above a critical flapping frequency, in this case $f=5.5$ ($\mathrm{Re}_f=55$, $\kappa=33$), where we capture the surprising direction reversal as observed in the experiments. Above this critical frequency, the wing travels backward in the direction away from the driving pivot point in a coherent and periodic manner. As in the experiments, we find that the transition regime from forward to backward locomotion is bistable, as indicated by the two values of mean horizontal velocity shown in Fig. 10 at $f=5.5$.

To illustrate, the sequence in Fig. 19 shows the onset of backward flapping flight for $f=5.5$. The body is initially ramped to a positive velocity so that $\dot{x}_0(t=0.5)=0.36$. For the first 15–18 periods the horizontal velocity does not vary significantly from the initial velocity, and the vortical structures on both sides of the wing are qualitatively similar. However, the strength of the vorticity produced at each end differs, and this discrepancy eventually leads to the selection of a backward moving state. After approximately 20 flapping periods, the body begins to accelerate to the left, until it eventually settles into an oscillatory steady state. We note that the passage and communication of leading edge to trailing edge vorticity in this flapping regime occur primarily on one side of the body, in this case along the upper surface. By symmetry, we expect that the system has chosen this state based on the initial conditions, and is equally likely to settle into a state with vorticity passage below the wing with equal likelihood over all initial conditions. In the steady state, the leading edge vorticity joins the trailing edge vorticity and detaches from the body with an upward orientation. Such vorticity patterns have been observed behind flapping bodies in experiments[37] and simulations,[30] even for clamped (nonpitching) wings.[13] The fluid wake to the right of the backward moving body once again takes the form of the reverse von Kármán street, with shed vortices aligned so that a fluid jet passes to the right, corresponding to leftward body thrust.

By seeding the body with a larger initial velocity, it is possible to force the body through the initial vorticity struc-

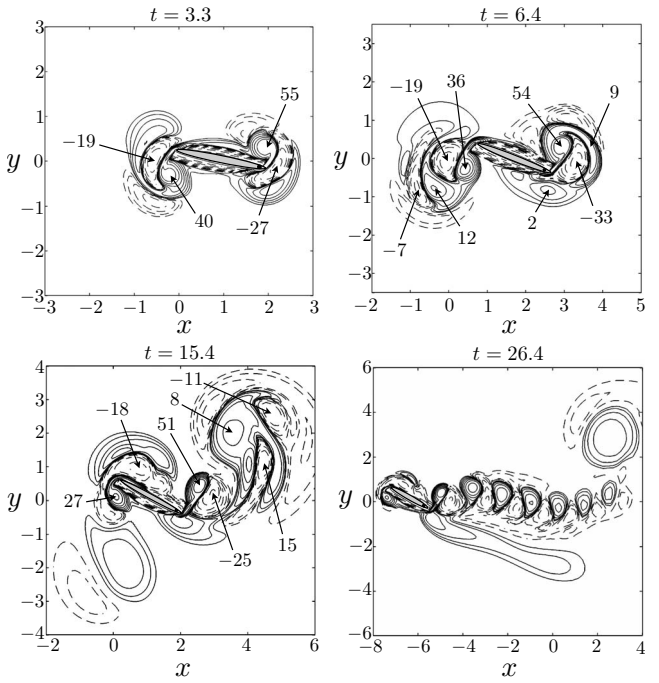

FIG. 19. Vorticity contours for a flapping wing initially ramped to a velocity $\dot{x}_0(t=0.5)=0.36$ at flapping frequency $f=5.5$. Contour values are the same as in Fig. 7. At $t=3.3$, the body rotates around a point near the centroid and sheds nearly left/right symmetric vortical patterns, but with different strengths. At $t=6.4$, the initial near-symmetry continues to break down. At $t=15.4$, the body is moving to the left and passes through the initial vorticity structure. By $t=26.4$, the body dynamics have reached a periodic steady state. The wake includes an up/down asymmetry.

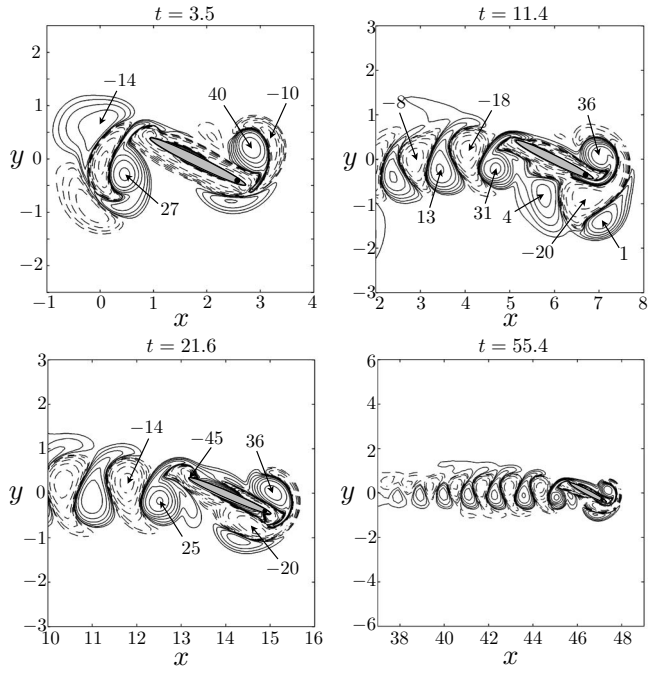

FIG. 20. Vorticity contours for a flapping wing initially ramped to a velocity $\dot{x}_0(t=0.5)=0.72$ at flapping frequency $f=5.5$. At $t=3.5$, the larger initial horizontal velocity drives the wing through the stronger LEV pair. At $t=11.4$, stronger vortices are still created at the leading edge, but are passing back into the wake at the trailing edge. At $t=21.6$, the trailing vorticity generated at the trailing edge has become stronger, and the body is accelerating. By $t=55.4$, the body dynamics have reached a steady state; the forward velocity is large enough to sustain the passage of LEVs back into the wake.

ture on the right until the body settles instead to a forward (rightward) moving oscillatory steady state. Figure 20 shows vorticity contours for a body smoothly ramped to a velocity $\dot{x}_0(t=0.5)=0.72$. Stronger vortices are created at the leading edge as in the previous case, but the initial velocity is large enough to allow for the quick passage of these relatively large LEVs back into the wake on the left. The body takes longer to settle into the apparently stable oscillatory steady state than in the previous example. The velocity profiles for both simulations are shown together in Fig. 21. The horizontal velocity of the forward moving body is seen to overshoot its final periodic steady state velocity. This behavior was observed in many other simulations and is not presently understood.

Figures 22(a) and 22(b) show phase diagrams relating the pitching angle θ and the vertical centroid displacement y_0 for both the forward (a) and backward (b) moving states presented above. In the forward moving example, after an initial ramping period, the body settles into a periodic orbit which is symmetric both in pitching angle and in vertical centroid position (indicated by a dark black line). The variation in the orbit's band thickness seen in Fig. 22(a) indicates that the pitching angle reaches nearly its final periodic state more rapidly than does the vertical centroid position. In the backward moving case, states at times $t\in[0,1]$ approach a similar orbit to that observed for the forward moving case. However, for times $t\in(1,4)$, the dynamics shift steadily in the vertical position y_0 and in the pitching angle. The dynamics settle into a shifted periodic orbit for $t\geq 4$. This shift corresponds to an up/down pitching asymmetry. The body spends more time with its centroid above the x-axis than below during its periodic cycle.

To further illustrate this surprising up/down asymmetry, the maximum and minimum pitching angles for a wider range of flapping frequencies are shown in Fig. 24. The pitching is symmetric for all forward moving wings: the wing achieves equal but opposite pitching on each half stroke. However, beyond the critical direction-reversal frequency $f=5.5$, we observe the onset of a pitching asymmetry

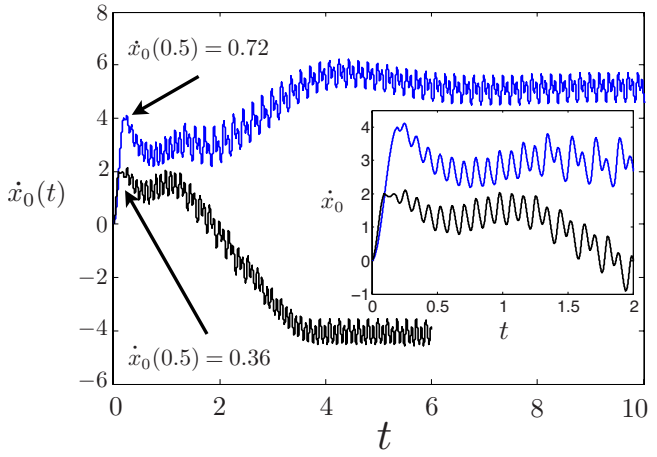

FIG. 21. (Color online) Horizontal velocities at flapping frequency $f=5.5$ for two seeded velocities, $\dot{x}_0(t=0.5)=0.72$ and $\dot{x}_0(t=0.5)=0.36$.

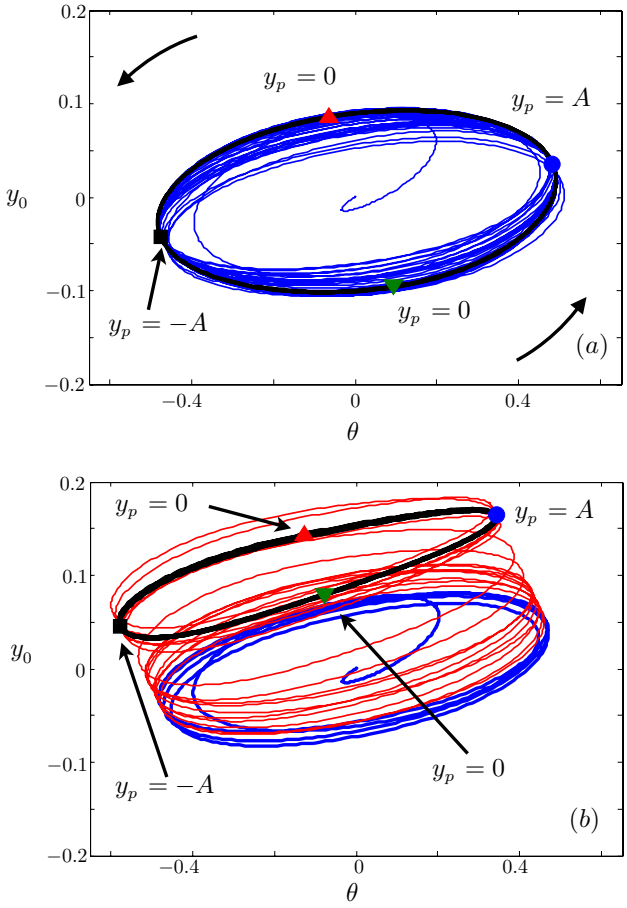

FIG. 22. (Color online) (a) Phase diagram relating the vertical position of the centroid $y_0(t)$ and the pitching angle $\theta(t)$ for the forward moving state shown in Fig. 19. A stable orbit is reached at approximately $t=6$ (see Fig. 21). Arrows indicate the direction of increasing time. Times ($t>4$) are shown as a dark black line. (b) The same diagram but for the backward moving state shown in Fig. 20. A transition occurs during $t\in[1,4]$ (thin line) to a periodic steady state for ($t>4$) (dark black line). The final periodic steady state has a positive mean vertical position and negative mean pitching angle, an up/down asymmetry noted in Fig. 19.

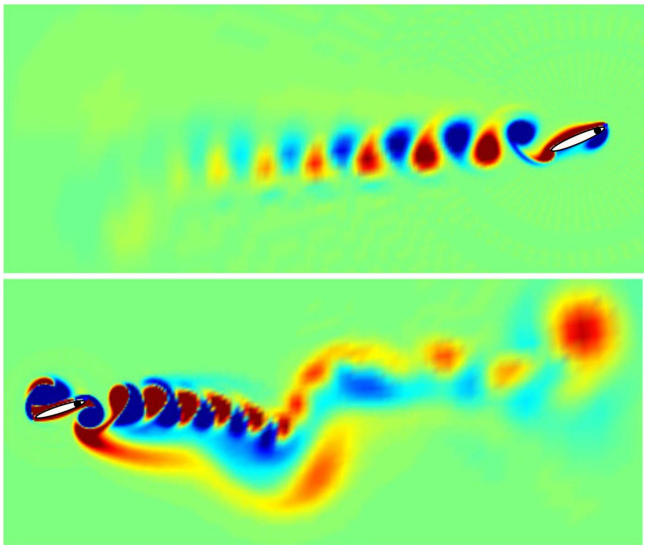

FIG. 23. (Color online) A direct comparison of the up/down symmetric vortical wake behind a forward moving wing (top), and an up/down asymmetric wake behind a backward moving wing (bottom). Both are driven vertically at the rightmost edge.

for all the backward moving states. This asymmetry in body orientation is accompanied by an up/down asymmetry in the wake, as seen in Fig. 19, and as shown in a more direct comparison with a forward moving state in Fig. 23. The pitching angle scales approximately as $\theta_{\max}\sim f^2$ in the first three regimes of flapping frequency (forward moving bodies), as shown in Fig. 24(b).

Other simulations showed more extreme deviations from mean-zero pitching deflection than in the current example; in those cases, the body plunges almost vertically during the heaving downstroke, then exhibits a backward motion while the pitching angle returns to nearly zero on the heaving upstroke. Subsequent to this numerical observation, the same pitching asymmetry was detected for the backward moving states in the experiments upon the introduction of a weaker torsional spring. An extreme example of the asymmetry is shown in the following section. At the bistable frequency ($f=5.5$) two sets of data points are included in Fig. 24, corresponding to the forward and backward moving states. The solid-colored points show the deflection angles for the backward moving state, and the asymmetry in the motion and its resultant vortical wake can be seen in Fig. 19. The forward moving state, however, still shows an up/down pitching symmetry, as seen in Fig. 20.

Phase diagrams relating the pitching angle θ to the centroid's vertical position y_0 are shown in Fig. 25 for a selection of flapping frequencies well after the ramp-up stage, $t\geq 3$. Times corresponding to the extrema and zeroes of the driving pivot's vertical displacement are marked. For flapping frequency $f=3$, at the pivot apex $y_p=A$, the pitching angle is already negative (the body has crossed the horizontal plane) and is increasing in magnitude, yielding large vertical displacements of the trailing edge. At the same time for $f=4$ the trailing edge is similarly moving upward, but has not yet crossed the horizontal plane when the pivot point begins its downward plunge. The body is "too flexible" for efficient locomotion and does not have enough time to present a large trailing edge vertical displacement to the flow before the body begins heaving in the opposite direction. The wing exhibits the backward moving state for $f=8$ and $f=16$ and there is a much smaller vertical centroid displacement, though the pitching angle varies with a similar range as for the forward motion case at $f=4$. For $f=8$ there is a slight shift to positive-mean pitching and negative-mean vertical displacement dynamics, the up/down asymmetry previously discussed. The center of mass has only a small vertical displacement and the phase relation is $\phi>\pi$. The direction of the orbit has also reversed in this backward moving state. That the orbit has reversed here but not in the backward moving case in Fig. 20 may be relevant to the bistability, but this requires further investigation. Finally, the orbit for $f=16$ is not stable and the body departs into irregular motion, which we discuss in the following section.

We refer again to Fig. 18 showing the phase difference ϕ, where the forward moving states are denoted by circles, and the backward moving states by squares. The backward moving states correspond to motion at heaving/pitching

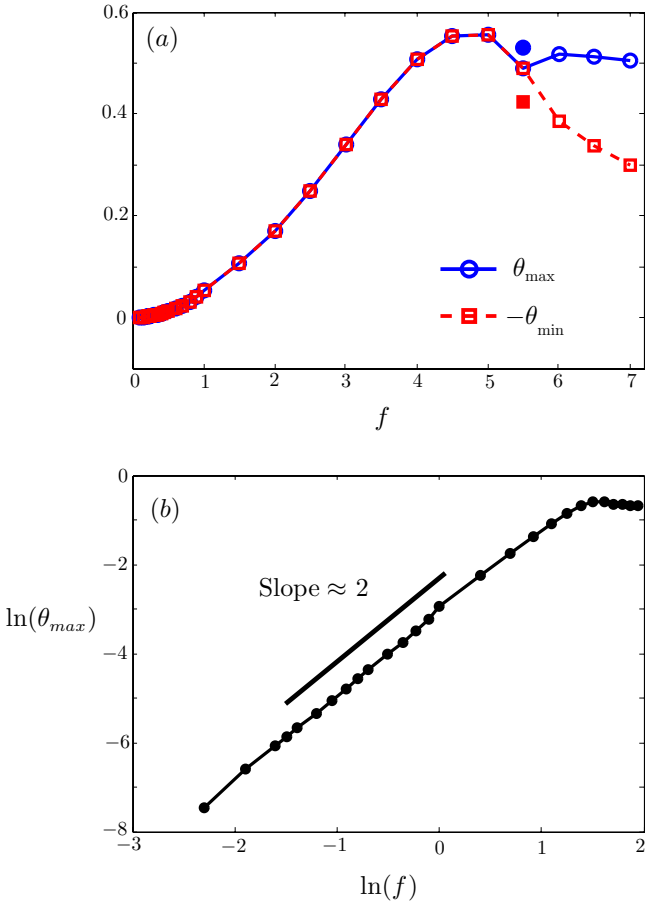

FIG. 24. (Color online) The maximum and (negative) minimum pitching angles on (a) linear and (b) logarithmic scales. The flapping dynamics for forward moving states are up/down symmetric. The solid data points in (a) correspond to the backward moving state at flapping frequency $f=5.5$.

phases $\phi > \pi$, corresponding to rotation around a point to the left of the center of mass as illustrated in Fig. 3(c). The wing's leftmost edge for phase differences $\phi > \pi$ undergoes larger vertical displacements than the vertically driven edge. The body then presents itself to the fluid with "leading" and

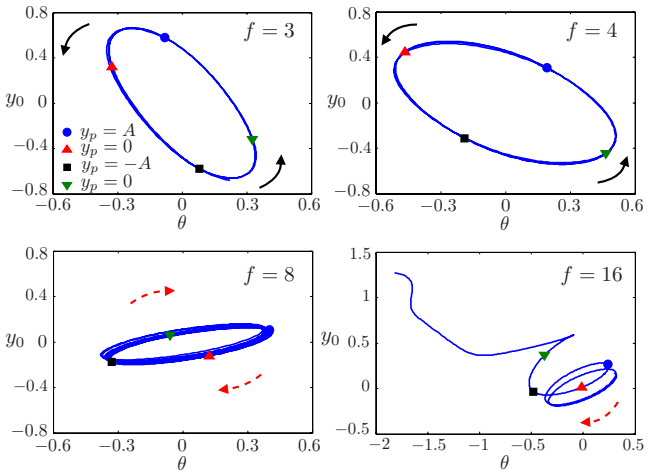

FIG. 25. (Color online) Phase diagrams relating the pitching angle $\theta(t)$ to the vertical position of the centroid $y_0(t)$ for a selection of flapping frequencies f. Arrows indicate the direction of increasing time.

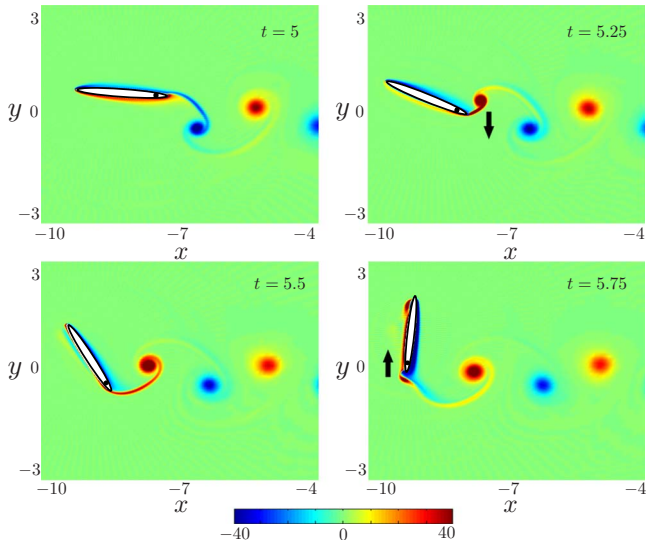

FIG. 26. (Color online) An extreme flapping frequency, $f=16$ ($\mathrm{Re}_f=160$, $\kappa=3.9$). At $t=5$ the body enters into another flapping cycle and by $t=5.5$ the pitching angle has crossed a critical threshold. As the driving pivot moves upward for the second half of the flapping stroke in $t \in (5.5,6)$, the body's major axis becomes aligned with the heaving direction.

"trailing" edges playing reversed roles. The simulations thus confirm the experimental results regarding the importance of heaving/pitching phase difference in determining the direction of lateral motion.

D. Extreme flapping yields highly irregular dynamics

For extremely large flapping frequencies, $f \gg 1$, the body exhibits highly irregular dynamics related to the pitching asymmetry discussed in the previous section. Figure 26 shows the flapping dynamics at flapping frequency $f=16$ ($\mathrm{Re}_f=160$, $\kappa=3.9$). Starting from rest, the body accelerates to the left (backward free flight) for $t \in (0,5)$. The body in-

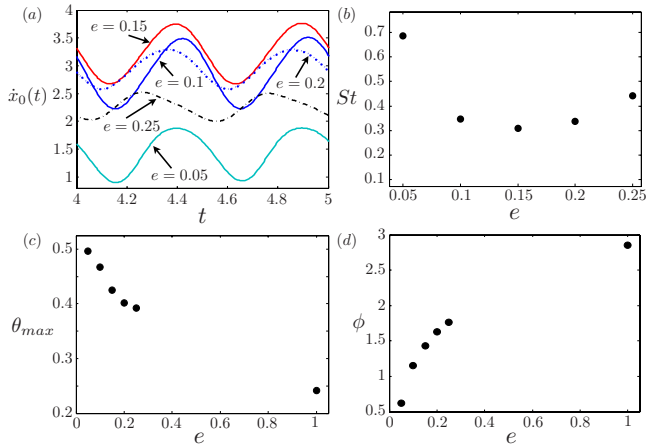

FIG. 27. (Color online) (a) Horizontal velocity profiles during one flapping period are shown for five different aspect ratios, with frequency Reynolds number $\mathrm{Re}_f=20$, spring constant $\kappa=25,250$, and mass $M=1.01$. (b) The Strouhal number is not monotonic in the aspect ratio and achieves a local minimum near $e=0.15$. (c) The maximum deflection angle as a function of the aspect ratio e for the coherent states. (d) The phase difference between heaving and pitching.

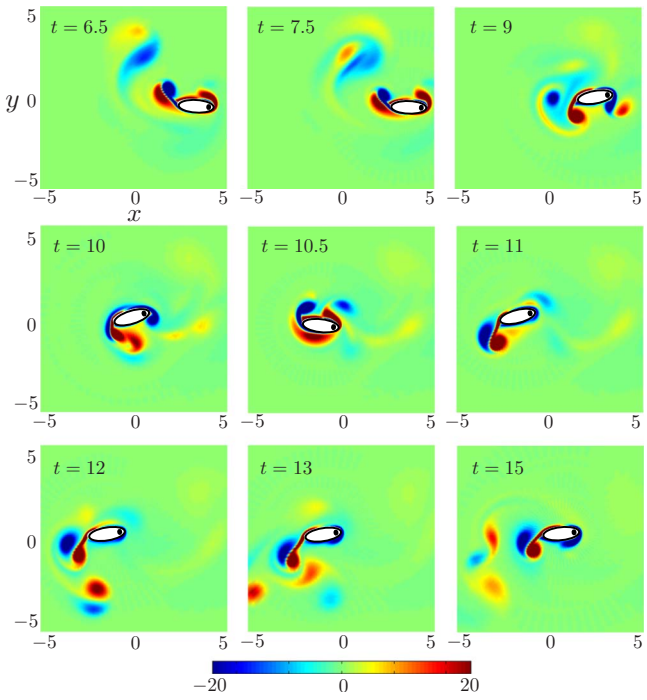

FIG. 28. (Color online) Vorticity profiles generated by a flapping body with aspect ratio $e=0.35$. The behavior is incoherent, and the body experiences large velocity bursts to the left and right.

ertia partially stabilizes the motion during the initial heaving periods, but there is a steady drift in the pitching angle so that the body spends more time tilted in one direction than in the other (the aforementioned up/down asymmetry). At $t=5$ the body begins another period, and at $t=5.25$ the heaving velocity is its most negative (as shown). Positive vorticity is shedding from the trailing edge on the right and the body is rotating with a negative angular velocity. At the heaving half period, $t=5.5$, the body is oriented with a dramatic pitching angle. While the heaving continues in the positive $\hat{\mathbf{y}}$ direction for $t\in(5.5,6)$, due to an unbalanced rotational inertia the body continues rotating past the vertical heaving axis. For $t>5.75$, the body begins to exhibit highly irregular dynamics.

The orientational alignment of the major axis to the heaving direction presented in Fig. 26 is reminiscent of the tumbling dynamics of falling paper, as simulated using a similar numerical method in Ref. 21. In that case gravity drives the system, and due to the drag anisotropy and the coupling of translational and rotational velocities, the body can glide into an upright position with an elevated center of mass. The role of the heaving pivot here is in that situation played by the body inertia.

V. COHERENCE TO INCOHERENCE, AND BACK AGAIN

Finally, we consider the dependence of the dynamics on the wing aspect ratio, e. A recent study by Zhang *et al.*[38] considered numerically the effect of aspect ratio of a flapping clamped wing (free to move horizontally with the fluid forces). There it was observed that the chord-thickness ratio can affect the symmetry-breaking bifurcation, the arrangement of vortices in the wake, and the terminal velocity of the wing. Other studies of a flapping clamped wing have shown that thinner bodies move more directly and smoothly into steady locomotion and exhibit a symmetry breaking instability at smaller frequency Reynolds number Re_f.[13] Figure 27(a) shows the horizontal velocities of wings with various aspect ratios at periodic steady states. Here, the frequency Reynolds number $\mathrm{Re}_f=20$, spring constant $\kappa=25,250$, and mass $M=1.01$ are fixed. We observe that the mean horizontal velocity is not monotonic in the aspect ratio. Correspondingly, Fig. 27(b) shows the dependence of the Strouhal number upon the aspect ratio e, and we find that $e\approx0.15$ maximizes the forward flight velocity in this setting.

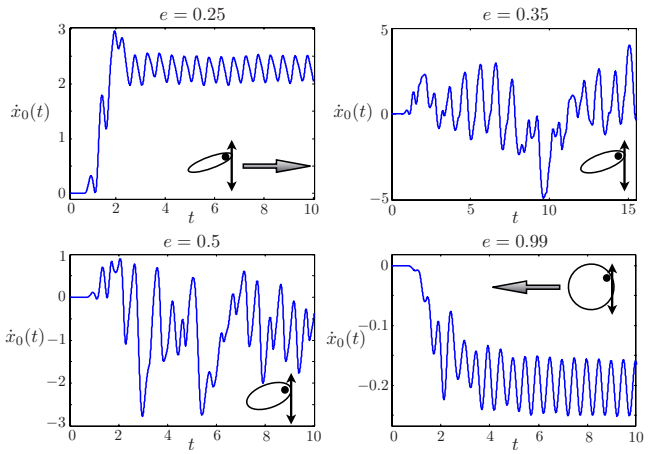

FIG. 29. (Color online) Horizontal velocity profiles for four aspect ratios e. Coherent forward motion transitions to incoherent dynamics as the aspect ratio is increased, but the body settles into a coherent backward motion for a nearly circular wing cross section.

Surprising dynamics are exhibited by a flapping body with aspect ratios $e\geq0.3$. The body exhibits a regime of incoherent, apparently chaotic behavior, before settling down again to a periodic steady state for bodies of nearly circular cross section, $e\approx1$. Figure 28 shows a selection of vorticity profiles for aspect ratio $e=0.35$. The body interacts strongly with previously shed vortices and exhibits highly irregular, possibly chaotic dynamics. At $t=10$ the body is plunging downward into previously shed positive vorticity, which imparts a large force on the body to the left (as in the simulations of Alben and Shelley).[13] There is clear breaking of up/down symmetry in this case, and vortex dipoles shed from the body shuttle fluid momentum away from the body in various directions. Large velocity bursts near $t=10$ and $t=15$ are seen in the horizontal velocity profile in Fig. 29(b), where we include the velocities of bodies with $e=0.25$, $e=0.5$, and $e=0.99$ for comparison.

Figures 27(c) and 27(d) show the maximum pitching angle and the heaving-to-pitching phase difference ϕ for this range of aspect ratios. The phase difference ϕ is not clearly defined for $e=0.35$ and $e=0.5$, but the trends in Figs. 27(c) and 27(d) which appear to carry through the incoherent regime indicate that some aspects of the dynamics are not randomized through the transition. For example, the pitching angle and the vertical displacement do not appear to vary dramatically, for even the chaotically moving bodies. Figure

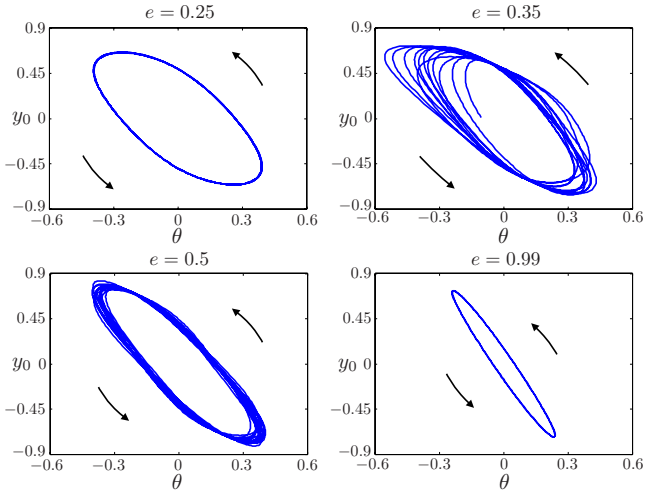

FIG. 30. (Color online) Phase diagrams relating the pitching angle θ to the centroid's vertical displacement y_0 for four aspect ratios e. The orbits for aspect ratios $e=0.35$ and $e=0.5$ do not appear to explore large regions of phase space. Arrows indicate the direction of time. (Ramp-up stages not shown.)

30 shows phase diagrams relating the pitching angle to the centroid's vertical displacement y_0 for the same four aspect ratios considered in Fig. 29. The orbits for aspect ratios $e=0.35$ and $e=0.5$ do not appear to explore large regions of phase space, though longer simulations will be considered in a future study. As we have shown in the previous sections, increased dimensionless flexibility can allow for certain asymmetries in the pitching dynamics, and we suggest that the irregular dynamics seen here can become even more incoherent in such cases.

While the velocity of the body with $e=0.35$ does not exhibit any coherent structure, a body with aspect ratio $e=0.5$ appears to be biased toward leftward (backward) motion. The phase diagram in Fig. 30 for the $e=0.5$ case indicates that the vertical and rotational components of the dynamics are not varying outside a tight band in phase space, but the fluid-body interaction and horizontal motion is still quite irregular as shown in Fig. 29. As a final unexpected result, we find that a flapping body with nearly circular cross section, $e=0.99$, settles once again into a coherent periodic steady state, but with a negative mean velocity. The vorticity generated by this flapping cylinder is shown in Fig. 31. The mean velocity is $\langle \dot{x}_0 \rangle = -0.20$, the maximum pitching angle is

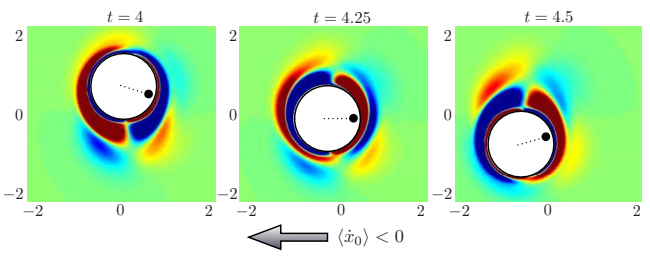

FIG. 31. (Color online) Vorticity generated by a flapping body with nearly circular cross section ($e=0.99$). The body settles into a coherent, backward-moving periodic steady state.

$\theta_{max}=0.24$ rad or 14°, and the heaving/pitching phase difference is $\phi=0.2871$ rad.

VI. CONCLUDING REMARKS AND FUTURE DIRECTIONS

We studied through experiment and numerical simulation an immersed flapping body which is free to pitch passively and move laterally. The experiments revealed a surprising reversal in the direction of lateral motion as the flapping increases beyond a critical frequency, and a bistable, hysteretic regime where the wing can move either forward or backward depending on its history. Characteristic of forward and backward motions are heaving-to-pitching phase differences $\phi<\pi$ and $\phi>\pi$, respectively, and the maximum pitching angle is observed to settle to a constant through the transition and for the backward moving wings.

The numerical simulations verified many of the experimental results. In addition, they have been used to predict new modes of locomotive behavior such as the up/down pitching asymmetry in the backward moving case, which was verified by subsequent experiments. The parameters selected to illustrate direction reversal and related behaviors were chosen to eliminate more complicated, unsteady dynamics. Future work will consider in more detail the effects of other parameters, such as body mass and inertial moment, flapping amplitude, a spring damping constant, and the driving pivot location.

While the experiments were performed at Reynolds numbers on the order of $\mathrm{Re}_f \sim 10^5$, the numerical simulations were performed at much smaller Reynolds numbers. The general properties of direction reversal have been captured here in the regime $\mathrm{Re}_f \sim 50$. This seems to indicate that it is sufficient for direction reversal that the Reynolds number is large enough to accommodate vortex shedding from the body into the surrounding fluid.[28] However, there are likely differences in the dynamics at these two regimes in Reynolds number, if possibly subtle. Namely, while we located an example of bistability, we have not thus far obtained a clear understanding of the large bistable regime observed in the experiments. We suspect that the separation in the Reynolds numbers may play a role in the exceedingly rapid transition from forward to backward motion in flapping frequency as determined by the simulations. Other parameters such as body mass, inertial moment, and flapping amplitude may also be important in determining the nature of this transition.

Large organisms such as birds and fish have developed flexible appendages for use in propulsion, and the results shown here further corroborate what is increasingly clear in the biological and engineering communities: that flexibility is a key component in flapping and undulatory forms of locomotion.[15–18] Elastic components can reduce the inertial work required to decelerate and reaccelerate the propulsive appendage.[18,39] Generally speaking, an effective wing or fin should flap on a time scale commensurate with the relaxation time of the elastic components of the structure; otherwise, the elasticity is either negligible or dominant, and in either case no performance improvement will result. In the experiments and simulations considered here, the lateral velocities

were largest when the flapping frequency was near the immersed system's resonant frequency.

Meanwhile, the resultant dynamics for flapping past the efficient regime have not been entirely understood, and the peculiar result of direction reversal may have other surprising consequences. For example, it may be possible that such dynamics are used by some organisms in braking (as suggested in Ref. 11). By flapping a tail-fin at a frequency associated with backward motion, a fish might maintain its direction but more rapidly come to rest. However, the authors are not aware of any specific examples of this braking dynamics found in nature. To this point, other interesting future work might include an examination of the direction reversal dynamics in the presence of a larger connected body or load.

The direction reversal regime imposes an important constraint on the utility of flexibility in flapping locomotion. Namely, for a given elasticity there is a limit on the speed which may be achieved by increasing the driving frequency. To achieve any greater speeds the flapping structure must be stiffened (i.e., E must be decreased by increasing the rigidity). Flying and swimming organisms can benefit from a brief period of increased wing/fin stiffness. Muscles are not only used to provide motive oscillation, but they can also provide this temporary extra stiffness through contraction ("active lengthening;" see Ref. 17). This suggests that the input power requirements will increase markedly during such locomotive bursts. The results of the present work provide part of the answer to a larger question in the biological community, that of the mechanical consequences of increased stiffness in the context of swimming; namely, the possibilities ranging from increased lateral velocities to backward or even chaotic motion based on the complex interactions with the surrounding fluid.

We presented numerical findings on five regimes of flapping dynamics with passive pitching, but we observed many other dynamical states, not discussed here, in other regions of parameter space. Some simulations have shown locomotory and wake behavior periodically varying of the order of ten flapping cycles, or even 100 flapping cycles. Up/down wake symmetry for forward motion can be broken in some cases, and the vortical wake can follow either a periodic or aperiodic meandering path away from the body (also observed in Refs. 13 and 37). In conclusion, the flapping of even a simply shaped body in a viscous fluid creates an important and complex physical system, and there is still much to learn.

ACKNOWLEDGMENTS

We thank Leif Ristroph for directing our attention to the 19th century work of Ettiene-Jules Marey during the preparation of this manuscript. This article is based on work presented at the APS/DFD meetings in sessions BH.00001(2007) and HJ.00005(2008). Funding from the Department of Energy Grant No. DE-FG02-88ER25053 and NSF Grant No. DMS-0821520 is gratefully acknowledged.

APPENDIX A: DRIVING FORCE

The driving force F_D may be written without direct reference to the body accelerations. We first write the vertical and angular accelerations as

$$\ddot{y}_0 = [(M-1)\pi e]^{-1}(F_D + F_y), \tag{A1}$$

$$\ddot{\theta} = [(M-2)I]^{-1}[\cos(\theta)F_D - \kappa\theta + T], \tag{A2}$$

where

$$F_y = \frac{1}{\mathrm{Re}_f}\hat{\mathbf{y}} \cdot \underline{\mathbf{R}} \int_0^{2\pi} \left(-\tilde{\mathbf{x}}^{\perp}\frac{\tilde{\omega}_\xi}{g_\xi} + \tilde{\mathbf{x}}_\eta \tilde{\omega} \right)\Big|_{\xi=0} d\eta, \tag{A3}$$

and T and I are defined in Eqs. (28) and (29). Twice differentiating the geometric identity $y_p = y_0 + \sin(\theta)$ yields the relation $\ddot{y}_p = \ddot{y}_0 - \sin(\theta)\dot{\theta}^2 + \cos(\theta)\ddot{\theta}$, and inserting the above expressions we find

$$F_D = Q(\theta)^{-1}\left\{ \ddot{y}_p + \sin(\theta)\dot{\theta}^2 - \frac{1}{(M-1)\pi e}F - \frac{\cos(\theta)}{(M-2)I}(-\kappa\theta + T) \right\}, \tag{A4}$$

where

$$Q(\theta) = \frac{1}{(M-1)\pi e} + \frac{\cos^2(\theta)}{(M-2)I}. \tag{A5}$$

APPENDIX B: CODE VALIDATION

As in Ref. 40, we test the code by considering a cylinder impulsively seeded with velocity u_0 at Reynolds number $\mathrm{Re} = \rho u_0 L/\mu = 100$. Figure 32(a) shows the computed azimuthal velocity as a function of the radial distance r along $\theta = \pi/2$ (a line perpendicular to the motion), as computed in simulations at time $t = 0.1$. For comparison we also included the potential flow solution for the dynamics outside the boundary layer, $u_\theta(r) = u_0/(1+r^2)$. A resolution of 128×128 grid points in the simulations return an excellent agreement

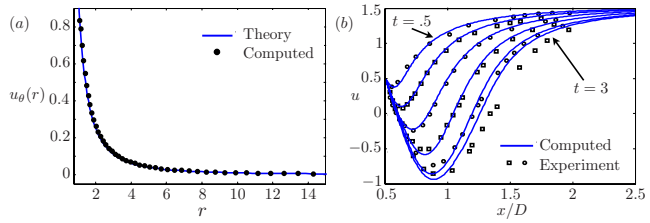

FIG. 32. (Color online) (a) The azimuthal velocity at $\theta = \pi/2$ is shown outside the boundary layer for an impulsively started cylinder at Reynolds number Re=100. (b) (Following Refs. 41 and 40) The horizontal velocity u at different locations along the symmetric axis (x/D) in the wake, where D is the diameter of the cylinder. Different symbols correspond to the time of measurements (scaled by D/u_0) with an increment of 0.5, starting from $t = 0.5$. Lines are from the numerics, and points are from the experiments of Ref. 41.

TABLE I. $\Delta\xi$ convergence.

N_1	$\dot{x}_0(3)$	$\theta(3)$	$\|\omega(\xi=0,\eta,t=3)\|_\infty$	$\hat{\mathbf{x}}\cdot\mathbf{F}_{\text{Fluid}}(t=3)$	$\hat{\mathbf{y}}\cdot\mathbf{F}_{\text{Fluid}}(t=3)$	$\tau_{\text{Fluid}}(t=3)$
80	−0.2165	0.4176	58.33	−0.2960	9.434	7.936
160	−0.2035	0.4158	58.91	−0.3180	9.573	8.123
320	−0.2024	0.4156	58.95	−0.3199	9.584	8.138
Ratio (R)	11.8	9	11.7	12.6	12.8	12.5

with the theoretical solution. Also following Wang[40] and Lewin and Hariri,[30] we plot the wake velocity in Fig. 32(b) for Re=550, and overlay our solution with experimental values as determined by Bouard and Coutanceau.[41] Here we used 512×256 grid points and an outer boundary 60 times the cylindrical radius from the body. The body is placed in a flow that ramps up smoothly from rest in $t\in[0,0.05]$ to a subsequently uniform velocity $u_0=1$. The agreement is generally quite good; discrepancies may be due to the fact that the experiments are only approximately two-dimensional, and due to differences in initial conditions.

1. $\Delta\xi$ convergence test

The boundary layer thickness at the body surface scales like $O(\text{Re}^{-1/2})$, which we must resolve to accurately determine the fluid forces on the body (see Ref. 32). In addition, when the grid is too coarse in the far field, the introduction of vorticity there can induce a numerical instability. Hence, it is desirable to use a large number of grid points in the radial direction, though this must be balanced with the increased computational time for simulation. We compare positions, velocities, surface vorticity, and fluid forces on the flapping wing at $t=3$ for three different N_1 (number of radial grid points), where $\Delta\xi=1/N_1$, and present the results in Table I. Here, we fix $\Delta t=.005$, $N_2=128$, $\text{Re}_f=10$, $M=1.01$, $e=0.2$, and $\kappa=1000$, and the far-field boundary is set 50 times the body length away from the wing surface. The forces and torque $\mathbf{F}_{\text{Fluid}}$ and τ_{Fluid} are defined in the text. Using the horizontal velocity as an example, the difference ratio is computed as

$$R=\frac{\dot{x}_0(t=3;\Delta\xi)-\dot{x}_0\left(t=3;\frac{\Delta\xi}{2}\right)}{\dot{x}_0\left(t=3;\frac{\Delta\xi}{2}\right)-\dot{x}_0\left(t=3;\frac{\Delta\xi}{4}\right)}, \tag{B1}$$

which returns $R\sim2^n$ asymptotically in $\Delta\xi\ll1$ for an nth order accurate numerical scheme.

TABLE II. $\Delta\eta$ convergence.

N_2	$\dot{x}_0(3)$	$\theta(3)$	$\|\omega(0,\eta,t=3)\|_\infty$	$\hat{\mathbf{x}}\cdot\mathbf{F}_{\text{Fluid}}(t=3)$
32	−0.2010	0.4157	53.81	−0.3209
64	−0.2028	0.4157	58.57	−0.3192
128	−0.2028	0.4157	58.93	−0.3192

Here we find difference ratios between 2^3 and 2^4, and we conclude that the numerical method is between third- and fourth-order accurate in $\Delta\xi$. The difference formulae used to compute derivatives were formally fourth order; however, the discretization of the vorticity's normal derivative on the body surface is only third-order accurate in general, due to the relationship between $\tilde{\omega}$ and $\tilde{\psi}$ there through Briley's formula.[20,24]

2. $\Delta\eta$ convergence test

We compare positions, velocities, surface vorticity, and fluid forces on the flapping wing at $t=3$ for three different numbers of azimuthal grid points N_2, where $\Delta\eta=2\pi/N_2$, and present the results in Table II. Here, we fix $\Delta t=.005$, $N_1=200$, $\text{Re}_f=10$, $M=1.01$, $e=0.2$, and $\kappa=1000$, and the far-field boundary is set 50 times the body length away from the wing.

The error converges rapidly as we decrease the azimuthal grid spacing $\Delta\eta$. In this case, 64 Fourier modes are sufficient so that errors are due only to radial and time discretizations.

3. Δt convergence test

By solving the system implicitly, we are not bound by the same stability constraints as for explicit schemes.[20] Thus, we are free to take a relatively large time step for our computations; for the simulations presented in the text, we used $\Delta t=.005$. To examine the convergence order, we choose parameters $N_1=100$, $N_2=64$, $M=1.01$, $e=0.2$, $\text{Re}_f=10$, and $\kappa=1000$, and compute to $t=2$ with varying the time-step size Δt. The far-field boundary is the same as in the previous test. There, we compare the ratios of computed final pitching angle and maximum surface vorticity, as discussed above, and the results are shown in Table III. The difference ratios indicate that the numerical scheme is second-order accurate in time.

TABLE III. Δt convergence.

Δt	$\theta(t=2)$	$\|\omega(0,\eta,t=2)\|_\infty$
0.005	−0.093 44	110.70
0.0025	−0.093 66	110.20
0.001 25	−0.093 72	110.07
Ratio	4.15	4.06

[1]M. Sfakiotakis, D. M. Lane, and J. B. C. Davies, "Review of fish swimming modes for aquatic locomotion," IEEE J. Ocean. Eng. **24**, 237 (1999).
[2]J. Lighthill, *Mathematical Biofluiddynamics* (SIAM, Philadelphia, 1975).
[3]*Swimming and Flying in Nature*, edited by T. Y.-T. Wu, C. J. Brokaw, and C. Brennen (Plenum, New York, 1975), Vol. 2.
[4]M. S. Triantafyllou, G. S. Triantafyllou, and D. K. P. Yue, "Hydrodynamics of fishlike swimming," Annu. Rev. Fluid Mech. **32**, 33 (2000).
[5]M. S. Triantafyllou, A. H. Techet, and F. S. Hover, "Review of experimental work in biomimetic foils," IEEE J. Ocean. Eng. **29**, 585 (2004).
[6]Z. J. Wang, "Dissecting insect flight," Annu. Rev. Fluid Mech. **37**, 183 (2005).
[7]E.-J. Marey, *Annual report of the Board of Regents of the Smithsonian Institution* (Smithsonian Institution, Washington, 1871).
[8]R. Gopalkrishnan, M. S. Triantafyllou, G. S. Triantafyllou, and D. Barrett, "Active vorticity control in a shear-flow using a flapping foil," J. Fluid Mech. **274**, 1 (1994).
[9]J. M. Anderson, K. Streitlien, D. S. Barrett, and M. S. Triantafyllou, "Oscillating foils of high propulsive efficiency," J. Fluid Mech. **360**, 41 (1998).
[10]F. S. Hover, O. Haugsdal, and M. S. Triantafyllou, "Effect of angle of attack profiles in flapping foil propulsion," J. Fluids Structures **19**, 37 (2004).
[11]D. A. Read, F. S. Hover, and M. S. Triantafyllou, "Forces on oscillating foils for propulsion and maneuvering," J. Fluids Struct. **17**, 163 (2003).
[12]N. Vandenberghe, J. Zhang, and S. Childress, "Symmetry breaking leads to forward flapping flight," J. Fluid Mech. **506**, 147 (2004).
[13]S. Alben and M. Shelley, "Coherent locomotion as an attracting state for a free flapping body," Proc. Natl. Acad. Sci. U.S.A. **102**, 11163 (2005).
[14]U. K. Muller, B. L. E. Van Den Heuvel, E. J. Stamhuis, and J. J. Videler, "Fish foot prints: Morphology and energetics of the wake behind a continuously swimming mullet (Chelon labrosus Risso)," J. Exp. Biol. **200**, 2893 (1997).
[15]M. E. DeMont, "Tuned oscillations in the swimming scallop *Pecten maximus*," Can. J. Zool. **68**, 786 (1990).
[16]W. M. Oxner, J. Quinn, and M. E. DeMont, "A mathematical model of body kinematics in swimming tadpoles," Can. J. Zool. **71**, 407 (1993).
[17]J. H. Long, Jr. and K. S. Nipper, "The importance of body stiffness in undulatory propulsion," Am. Zool. **36**, 678 (1996).
[18]D. A. Pabst, "Springs in swimming animals," Am. Zool. **36**, 723 (1996).
[19]W. R. Sears, "Some aspects of non-stationary airfoil theory and its practical application," J. Aeronaut. Sci. **8**, 104 (1941).
[20]W. E and J. G. Liu, "Essentially compact schemes for unsteady viscous incompressible flows," J. Comput. Phys. **126**, 122 (1996).
[21]U. Pesavento and Z. J. Wang, "Falling paper: Navier-Stokes solutions, model of fluid forces, and center of mass elevation," Phys. Rev. Lett. **93**, 144501 (2004).
[22]S. E. Spagnolie and M. J. Shelley, "Shape-changing bodies in fluid: Hovering, ratcheting, and bursting," Phys. Fluids **21**, 013103 (2009).
[23]Z. J. Wang, "Efficient implementation of the exact numerical far field boundary condition for Poisson equation on an infinite domain," J. Comput. Phys. **153**, 666 (1999).
[24]S. Alben, "An implicit method for coupled flow-body dynamics," J. Comput. Phys. **227**, 4912 (2008).
[25]W. R. Briley, "A numerical study of laminar separation bubbles using the Navier-Stokes equations," J. Fluid Mech. **47**, 713 (1971).
[26]W. E and J. G. Liu, "Vorticity boundary condition and related issues for finite difference schemes," J. Comput. Phys. **124**, 368 (1996).
[27]Y. Saad and M. H. Schultz, "GMRES—a generalized minimal residual algorithm for solving nonsymmetric linear-systems," SIAM (Soc. Ind. Appl. Math.) J. Sci. Stat. Comput. **7**, 856 (1986).
[28]L. A. Miller and C. S. Peskin, "When vortices stick: An aerodynamic transition in tiny insect flight," J. Exp. Biol. **207**, 3073 (2004).
[29]M. M. Koochesfahani, "Vortical patterns in the wake of an oscillating airfoil," AIAA J. **27**, 1200 (1989).
[30]G. C. Lewin and H. Haj-Hariri, "Modelling thrust generation of a two-dimensional heaving airfoil in a viscous flow," J. Fluid Mech. **492**, 339 (2003).
[31]H. Dong, R. Mittal, and F. M. Najjar, "Wake topology and hydrodynamic performance of low-aspect-ratio flapping foils," J. Fluid Mech. **566**, 309 (2006).
[32]G. K. Batchelor, *Introduction to Fluid Dynamics* (Cambridge University Press, Cambridge, 1967).
[33]G. S. Triantafyllou, M. S. Triantafyllou, and M. A. Grosenbaugh, "Optimal thrust development in oscillating foils with application to fish propulsion," J. Fluids Structures **7**, 205 (1993).
[34]G. K. Taylor, R. L. Nudds, and A. L. R. Thomas, "Flying and swimming animals cruise at a Strouhal number tuned for high power efficiency," Nature (London) **425**, 707 (2003).
[35]E. M. Purcell, "Life at low Reynolds-number," Am. J. Phys. **45**, 3 (1977).
[36]E. Lauga, "Continuous breakdown of Purcell's scallop theorem with inertia," Phys. Fluids **19**, 061703 (2007).
[37]S. Heathcote and I. Gursul, "Jet switching phenomenon for a periodically plunging airfoil," Phys. Fluids **19**, 027104 (2007).
[38]X. Zhang, S. Ni, S. Wang, and G. He, "Effects of geometric shape on the hydrodynamics of a self-propelled flapping foil," Phys. Fluids **21**, 103302 (2009).
[39]T. L. Daniel, in *Efficiency and Economy in Animal Physiology*, edited by R. W. Blake (Cambridge University Press, Cambridge, 1991), pp. 83–95.
[40]Z. J. Wang, "Vortex shedding and frequency selection in flapping flight," J. Fluid Mech. **410**, 323 (2000).
[41]R. Bouard and M. Coutanceau, "The early stage of development of the wake behind an impulsively started cylinder for $40 < \mathrm{Re} < 104$," J. Fluid Mech. **101**, 583 (1980).